DØ Note 4795 (v4.13)

Measurement of the Ratio of the $Z/\gamma^*(\rightarrow e^+e^-)+\geq n$ Jet Production Cross Sections to the Total Inclusive $Z/\gamma^* \rightarrow e^+e^-$ Cross Section in $p\bar{p}$ Collisions at $\sqrt{s} = 1.96$ TeV

Marc Buehler, James Heinmiller, Alan Stone, Nikos Varelas

Abstract

We present a study of events with Z bosons and hadronic jets produced at the Tevatron in $p\bar{p}$ collisions at a center of mass energy of 1.96 TeV. The data consist of approximately 14,000 $Z/\gamma^* \rightarrow e^+e^-$ decay candidates from 343 pb^{-1} of integrated luminosity collected using the DØ detector. Cross section ratios and jet production properties have been measured for $Z/\gamma^*+\geq 0$ to 4 jet events. We find our results in good agreement with QCD predictions.

Contents

1 Introduction

Signatures of the leptonic decays of electroweak gauge bosons, $W^{\pm}$ and Z, in association with jets are among the most prominent processes at hadron colliders. The measurements of $W/Z+ \geq n$ jets cross sections are important for studying perturbative QCD calculations and for understanding the QCD background to other interesting physics processes, within or beyond the Standard Model (SM).

For example, the most promising modes for a light Higgs discovery at the Tevatron are those where the Higgs is produced in association with a vector boson $(W/Z)H$ with $(W/Z) \rightarrow$ leptons and $H \rightarrow b\bar{b}$; the W+3/4 jets channel in which at least one jet was identified as a b-quark is important for top-quark studies; many extensions of the SM predict new particles which decay into SM gauge bosons and are accompanied by jets.

In this study we present a measurement of the $Z(e^+e^-)+ \geq n$ jets cross sections for jet multiplicities of $n \geq 0 - 4$ jets in $\sqrt{s} = 1.96$ TeV $p\bar{p}$ collisions using a 343 pb^{-1} data sample accumulated by the DØ detector. Our results are compared to QCD predictions.

2 Data Sample

The data sample used for this analysis was collected between April 2002 and June 2004 and contains approximately 876 million events [1]. The raw data are processed with the p14 version of the DØ reconstruction software. A calorimeter noise suppression algorithm (T42 [2]) is applied. In order to create a final data sample of manageable size, pre-selection or *skimming* criteria are used:

EM1TRK skimming Each event in the data set is required to have at least one EM object with ID = 10 or ±11, $p_T > 8$ GeV, and a track with $p_T >$ 5 GeV within $\Delta\phi = 0.1$ of the EM object. These requirements reduce the size of the data sample to approximately 57 million events.

Root-tuple creation The reconstructed data are reformatted into an object oriented ntuple format (*root-tuple*) using the ATHENA [3] software package (version p16-br-03). At this stage, JES corrections (version 5.3) are applied.

Root-tuple skimming The root-tuple data are further skimmed by requiring at least one EM object with EM fraction > 0.9, Isolation< 0.15, H-Matrix(7)< 12.0, $|\eta_{det}| < 1.1$ and a track match[1] in each event. The final analysis root-tuple contains 2.4 million events.

Data flagged as unusable by data-quality experts are excluded from the analysis. SMT, CFT, calorimeter, and luminosity subsystems of the detector are required to be fully operational. Additionally, all data taking periods with limited L1CAL trigger coverage ($|\eta| < 0.8$) are excluded [4].

[1] χ^2 probability for best track using the spatial distance in η and Φ and the E/p ratio.

Events for the analysis are selected based on the requirement that the trigger system identified at least one EM object (*single electron triggers*). Only *unprescaled* single electron triggers were used.

The data taking period for this analysis can be divided into two periods during which different lists of single EM triggers were implemented. The following is the prioritized order of trigger combinations for trigger lists before *global_CMT-12* (runs $\leq$ 178732, "pre-v12 dataset")[2] [5]:

- EM_HI_SH or EM_HI_2EM5_SH
- EM_HI_SH
- EM_HI
- EM_MX_SH
- EM_MX,

The trigger combinations for trigger list *global_CMT-12* (runs $\geq$ 178722, "v12 dataset") are:

- E1_SHT20 or E2_SHT20 or E3_SHT20 or E1_SH30
- E1_SHT20 or E2_SHT20 or E1_SH30
- E1_SHT20 or E1_SH30
- E1_SHT20,

Table 1 contains details of the individual triggers.

A total integrated luminosity of 343 pb^{-1} was available for this analysis after trigger selection and exclusion of unusable data due to bad quality.

3 Monte Carlo Samples

3.1 PYTHIA and ALPGEN Samples

The MC samples used for data comparisons and acceptance estimations are summarized in Table 2. For studies regarding the inclusive $Z/\gamma^* \to e^+e^-$ cross section, a PYTHIA [6] $Z/\gamma^* \to e^+e^-$ inclusive sample is used (CTEQ5L PDF). For higher jet multiplicities, events are generated with ALPGEN [7] and then passed through PYTHIA for parton showering and hadronization (CTEQ5L PDF, $\mu^2_{R/F} = M_Z^2 + \sum p^2_{T,jet}$).

The electron energy resolution measured in data is not correctly modeled by the MC simulation. Additional energy smearing is applied to the MC electrons to account for the difference. p_x, p_y, p_z and energy of the electrons are multiplied

[2] The statement "Trigger A or Trigger B" refers to the fact that a given event is accepted if Trigger A and Trigger B are unprescaled, and the trigger requirements for either Trigger A or Trigger B are met.

Trigger	L1	L2	L3
EM_HI_SH	CEM(1,10)	EM(1,12)	ELE_LOOSE_SH_T(1,20)
EM_HI_2EM5_SH	CEM(2,5)	EM(1,12)	ELE_LOOSE_SH_T(1,20)
EM_HI	CEM(1,10)	EM(1,12)	ELE_LOOSE(1,30)
EM_MX_SH	CEM(1,15)	none	ELE_LOOSE_SH_T(1,20)
EM_MX	CEM(1,15)	none	ELE_LOOSE(1,30)
E1_SHT20	CEM(1,11)	none	ELE_NLV_SHT(1,20)
E2_SHT20	CEM(2,6)	none	ELE_NLV_SHT(1,20)
E3_SHT20	CEM(1,9)CEM(2,3)	none	ELE_NLV_SHT(1,20)
E1_SH30	CEM(1,11)	none	ELE_NLV_SH(1,30)

L1 Triggers

CEM(1,10)	one EM trigger tower with $E_T > 10$ GeV
CEM(2,5)	two EM trigger towers with $E_T > 5$ GeV
CEM(1,15)	one EM trigger tower with $E_T > 15$ GeV
CEM(1,11)	one EM trigger tower with $E_T > 11$ GeV
CEM(2,6)	two EM trigger towers with $E_T > 6$ GeV
CEM(1,9)CEM(2,3)	one EM trigger tower with $E_T > 9$ GeV, another EM trigger tower with $E_T > 3$ GeV

L2 Triggers

EM(1,12)	one EM candidate with $E_T > 12$ GeV (not present for runs before 169524)

L3 Triggers

ELE_LOOSE_SH_T(1,20)	one electron with $\|\eta\| < 3.0$ and $E_T > 20$ GeV passing loose requirements including shower shape cuts
ELE_LOOSE(1,30)	one electron with $\|\eta\| < 3.0$ and $E_T > 30$ GeV passing loose requirements
ELE_NLV_SHT(1,20)	one electron with $\|\eta\| < 3.6$ and $E_T > 20$ GeV passing tight shower shape cuts
ELE_NLV_SH(1,30)	one electron with $\|\eta\| < 3.6$ and $E_T > 30$ GeV passing loose shower shape cuts

Table 1: Single EM triggers used in this analysis.

Process	Generators	Size
$Z/\gamma^* \to e^+e^-$	PYTHIA	400k
$Z/\gamma^* j \to e^+e^- j$	ALPGEN + PYTHIA	150k
$Z/\gamma^* jj \to e^+e^- jj$	ALPGEN + PYTHIA	180k
$Z/\gamma^* jjj \to e^+e^- jjj$	ALPGEN + PYTHIA	15k

Table 2: List of Monte Carlo samples

Coefficient	$\lvert\eta_{det}\rvert < 0.5$	$0.5 < \lvert\eta_{det}\rvert < 1.0$	$1.0 < \lvert\eta_{det}\rvert < 1.5$	$\lvert\eta_{det}\rvert > 1.5$
N_{data}	5.05	0	2.24	6.42
S_{data}	0.753	1.2	0.924	0
C_{data}	0.0893	0.087	0.135	0.0974
N_{MC}	4.26	4.61	3.08	4.83
S_{MC}	0.658	0.621	0.816	0
C_{MC}	0.0436	0.0578	0.0729	0.0735

Table 3: Jet energy resolution parameters (data and MC).

by $c \cdot \text{Gauss}(1, f)$, where Gauss(1,$f$) is the additional smearing parameter which is chosen from a Gaussian distribution with mean 1 and width f, and c is an overall calibration factor. The following values for the smearing parameters are used [8]:

- f = 0.045
- c = 1.003,

We also adjust the jet energy resolution in MC to match the jet resolution in data [9]. The parameterization of the jet energy resolution is given by:

$$\frac{\sigma(p_T)}{p_T} = \sqrt{\frac{N^2}{p_T^2} + \frac{S^2}{p_T} + C^2}, \tag{1}$$

where the constants C, S, and N represent the gain fluctuations, sampling fluctuations, and noise contributions respectively. Table 3 summarizes all coefficients for different detector regions. Figures 1 and 2 show the jet p_T resolutions for different η_{det} regions in data and MC, respectively.

Using the p_T and η_{det} of the MC jets, the data and MC resolutions are calculated. If the data resolution is better than the MC resolution for a given jet, no additional smearing is applied. If the jet resolution in data is worse than in MC, the MC jet energy resolution is adjusted by applying a multiplicative smearing factor (Equation 2) to the 4-vector components of each jet.

$$\text{Smearing Factor} = \text{Gauss}\left(1, \sqrt{\left(\frac{\sigma(p_T)}{p_T}\right)^2_{data} - \left(\frac{\sigma(p_T)}{p_T}\right)^2_{MC}}\right) \tag{2}$$

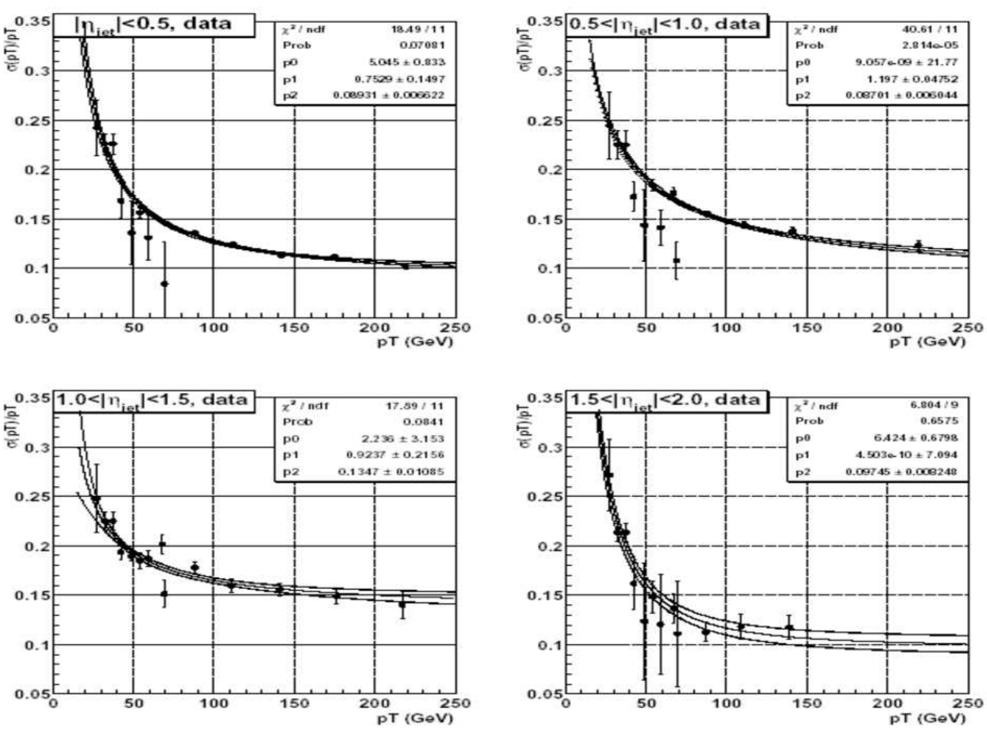

Figure 1: Jet p_T resolutions for different η_{det} regions in data (JES 5.0 with T42).

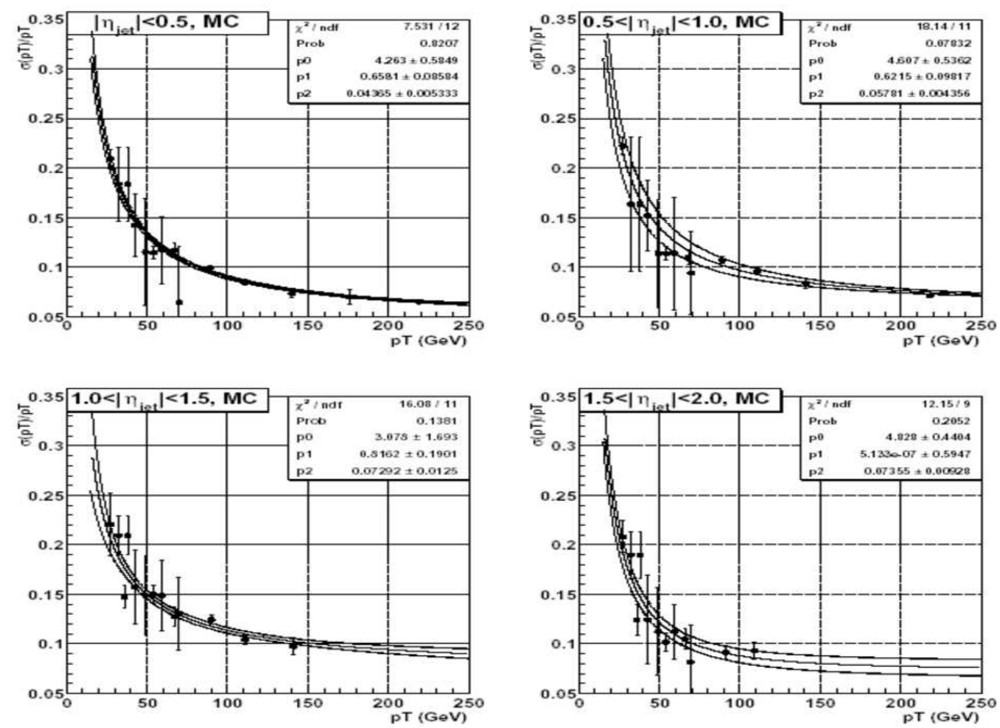

Figure 2: Jet p_T resolutions for different η_{det} regions in MC (JES 5.0 with T42).

3.2 CKKW Samples

MADGRAPH [10] is a tree-level matrix element generator, and it is based on specifying initial and final state particles for any tree level SM process. It creates a list of all relevant Feynman diagrams and calculates the corresponding matrix elements. The program is able to calculate matrix elements for any SM process. The only limitation is processing power. The MADGRAPH output is interfaced with PYTHIA for showering and hadronization.

The matching between MADGRAPH and PYTHIA to avoid double counting when combining different multiplicity final states is done following a modified CKKW prescription [11], [12], [13]. These samples are referred to as *CKKW samples* (Table 4).

The samples use a matching threshold of $p_T > 15$ GeV. Partons are generated with $|\eta| < 2.5$. The Z boson has a generated mass between 75 GeV and 105 GeV. The matrix element generation with MADGRAPH was done up to jet multiplicities of 3. Higher jet multiplicities are from parton showering simulated by PYTHIA. The factorization scale is set to $\mu_F^2 = M_Z^2$. The renormalization scale is set to $\mu_R^2 = p_{Tjet}^2$ for jets from initial state radiation and $\mu_R^2 = k_{Tjet}^2$ for jets from final state radiation.

Process	Generators	Size
$Z/\gamma^* j \to e^+e^- j$	MADGRAPH + PYTHIA	234k
$Z/\gamma^* jj \to e^+e^- jj$	MADGRAPH + PYTHIA	20k
$Z/\gamma^* jjj \to e^+e^- jjj$	MADGRAPH + PYTHIA	3k

Table 4: List of CKKW samples

3.3 MCFM Cross Sections

MCFM (*Monte Carlo for FeMtobarn processes*) can calculate inclusive parton level cross sections for $Z/\gamma^*(\to e^+e^-)$ at NLO in α_s for up to two partons in the final state [14],[15],[16]. The kinematic and geometric jet cuts are the same as used in the analysis: parton $p_T > 20$ GeV, $|\eta| < 2.5$. The Z boson has a mass between 80 GeV and 100 GeV, and CTEQ6M was selected for the PDF. The renormalization and factorization scales are set to $\mu_{F/R}^2 = M_Z^2$.

3.4 MC Background Samples

Additional backgrounds due to $W \to e\nu$, $Z \to \tau\tau$, and $t\bar{t} \to l\nu bl\nu b$ processes were studied using the MC samples listed in Table 5.

4 Event Selection

The following selection criteria are applied in order to assure that events with two high p_T electrons contained within the central calorimeter and originating

Process	Generators	Size
$W \to e\nu$	PYTHIA	245k
$Z \to \tau\tau$	PYTHIA ($60 < m_Z < 130$)	403k
$t\bar{t} \to l\nu bl\nu b$	ALPGEN + PYTHIA	154k

Table 5: List of background samples

from the decay of a Z/γ^* gauge boson are selected. After identifying the Z *candidate* events, the presence of $n > 0$ high p_T jets is required.

4.1 Primary Vertex

The efficiency to reconstruct the PV is $\approx 100\%$ in the central region of the detector, and decreases outside of the SMT fiducial volume. Therefore, the PV is required to be within 60 cm of the detector center along the beam pipe (z-axis).

4.2 Electron Selection

EM objects have to satisfy the following requirements:

- Loose electrons:
  - ID = 10 or ± 11: All EM clusters are assigned an ID of 10. If in addition a cluster has a track loosely matched (in η and Φ) to it, it is assigned an ID of ± 11 ("+" for electrons, "−" for positrons).
  - EM Fraction > 0.9: The electromagnetic fraction (EM fraction) discriminates between EM and hadronic calorimeter energy deposits. It takes advantage of the fact that EM showers are almost entirely contained within the EM layers of the calorimeters. EM fraction is defined as:
$$EMfraction = \frac{E_{EM}(R < 0.2)}{E_{tot}(R < 0.2)}, \tag{3}$$
where $E_{EM}(R < 0.2)$ is the EM energy within a cone of radius $R < 0.2$ (based on EM layers), and $E_{tot}(R < 0.2)$ is the total energy within a cone of radius $R < 0.2$ (based on EM, FH, and CH layers).
  - Isolation < 0.15: EM clusters are tested for *isolation*:
$$Isolation = \frac{E_{tot}(R < 0.4) - E_{EM}(R < 0.2)}{E_{EM}(R < 0.2)}, \tag{4}$$
where $E_{EM}(R < 0.2)$ is the EM energy within a cone of radius $R < 0.2$ (based on EM layers), and $E_{tot}(R < 0.4)$ is the total energy within a cone of radius $R < 0.4$ (based on EM, FH, and CH layers).

- H-Matrix(7) < 12: The H-Matrix distinguishes between EM and hadronic energy deposits, by analyzing the longitudinal and transverse shape of the showers. Based on MC generated electrons, a covariance matrix (M) is defined using a set of seven discriminant variables :

$$M_{ij} = \frac{1}{N} \sum_{n=1}^{N} (x_i^n - \langle x_i \rangle)(x_j^n - \langle x_j \rangle), \tag{5}$$

  where x_i^n is the value of variable i for electron n, and $\langle x_i \rangle$ is the mean value of variable i. The seven variables that are used are listed below:

  * Shower energy fraction in 1^{st}, 2^{nd}, 3^{rd}, and 4^{th} EM layer of the calorimeter.
  * Cluster size in $r - \Phi$ based on the 3^{rd} EM layer of the calorimeter[3].
  * Total shower energy.
  * Primary vertex position.

  The H matrix is defined as the inverse of the covariance matrix M:

$$H \equiv M^{-1}. \tag{6}$$

  Using the H matrix a χ^2-like variable is calculated that gives a measure of the likelihood that a given shower k is consistent with an EM object shower:
- $p_T > 25$ GeV
- $|\eta_{det}| < 1.1$.

• Tight electrons:

  - Requirements of loose electron.
  - Track match[4] with $P(\chi^2) > 0.01$.

4.3 Z Selection

Z candidates are selected based on the following criteria:

• Two loose electrons.

• At least one of the two electrons needs to be tight.

• One of the two electrons must have fired the trigger[5].

• Diem invariant mass window cut: 75 GeV < M_{ee} < 105 GeV.

[3] EM showers typically deposit the bulk of their energy in the 3^{rd} EM layer.
[4] χ^2 probability for best track using the spatial distance in η and Φ and the E/p ratio.
[5] Matching trigger objects at L1, L2, and L3 within $\Delta R < 0.4$ are required.

Sample	N	Fraction
$Z/\gamma^* + 0$ jets	12,247	0.8815
$Z/\gamma^* + 1$ jets	1,427	0.1027
$Z/\gamma^* + 2$ jets	189	0.0136
$Z/\gamma^* + 3$ jets	25	0.0018
$Z/\gamma^* + 4$ jets	3	0.0002
$Z/\gamma^* + 5$ jets	2	0.0001
Total	13,893	1.0000

Table 6: Event breakdown by exclusive jet multiplicities associated with Z/γ^* production before any background is subtracted or any corrections are applied.

4.4 Jet Selection

Jets are formed using the Run II Midpoint Jet Cone Algorithm with a cone size of 0.5 and are selected based on the following criteria:

- $0.05 < \mathrm{EMF} < 0.95$
- $\mathrm{HotF} < 10.$
- $\mathrm{N90} > 1.$
- $\mathrm{CHF} < 0.4$
- L1 confirmation
- JES corrected $p_T > 20$ GeV
- $|\eta_{physics}| < 2.5$
- Since the jet algorithm identifies *fake* jets originating from electron energy deposits, all jets overlapping with electrons coming from the Z/γ^* boson within $\Delta R = \sqrt{\Delta\eta^2 + \Delta\phi^2}$ of 0.4 are removed.

4.5 Event Statistics

Table 6 summarizes the number of $Z/\gamma^* \to e^+e^-$ event candidates for different exclusive jet multiplicities.

5 Data vs Monte Carlo

This section presents a comparison of basic kinematic distributions for electrons, Z candidates, and jets between data and MC simulations[6]. It is important that the MC distributions describe the data distributions as accurately as possible. The MC simulations are used to account for the fraction of events that are lost

[6] The MC distributions are normalized to the number of events in data.

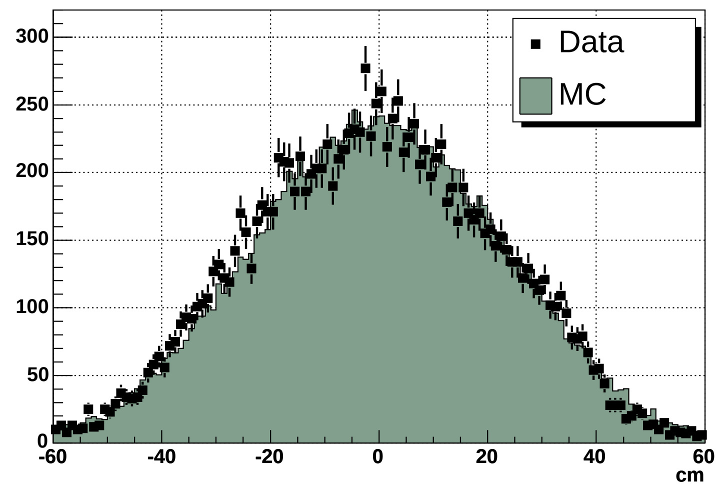

Figure 3: Primary vertex distribution in data and MC (PYTHIA) for the inclusive sample. The MC distribution is normalized to the number of events in data.

due to kinematic and geometric electron cuts, the diem invariant mass cut, and the primary vertex cut (*acceptance*).

5.1 Primary Vertex Comparison

Figure 3 compares the primary vertex distribution between data and inclusive $Z/\gamma^* \to e^+e^-$ PYTHIA MC.

5.2 Z p_T Comparisons

Figure 4 shows the Z p_T comparison between data and inclusive $Z/\gamma^* \to e^+e^-$ PYTHIA MC. Since PYTHIA is a LO ($2 \to 2$) generator at the hard process, there is disagreement in the Z p_T distribution (especially at high p_T) between data and MC. To account for this discrepancy, an additional corrective weight based on the Z p_T comparison between data and MC is applied to the MC electron and Z distributions. The Z p_T correction is also shown in Figure 4.

Figure 5 shows the Z p_T comparison when using PYTHIA MC after applying the Z p_T correction. Figures 6 and 7 show Z p_T comparisons when using ALPGEN for $Z+\geq 1$ jet and $Z+\geq 2$ jet samples. The agreement between ALPGEN + PYTHIA MC and data is deemed acceptable. Therefore, no additional Z p_T correction is applied to the ALPGEN + PYTHIA MC samples.

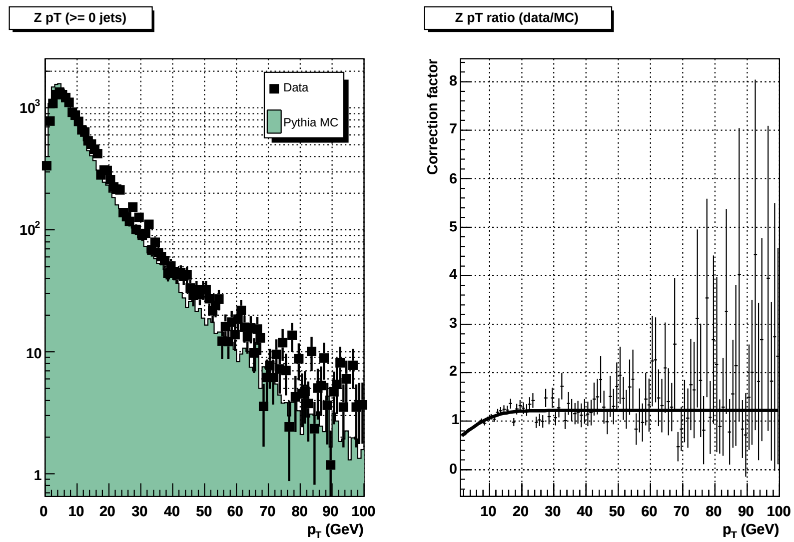

Figure 4: Comparison of Z p_T between data and PYTHIA MC (left), and ratio correction factor (right) for the inclusive sample. The MC distribution (left) is normalized to the number of events in data.

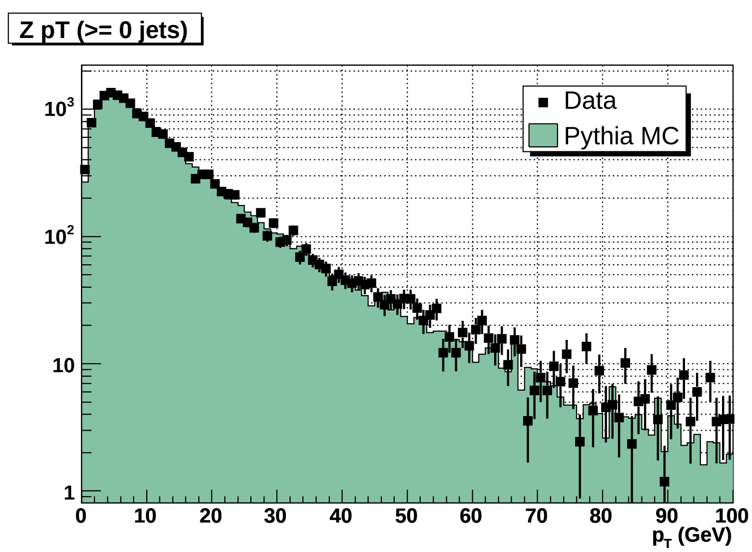

Figure 5: Comparison of Z p_T between data and PYTHIA MC after applying Z p_T correction. MC is normalized to the number of events in data.

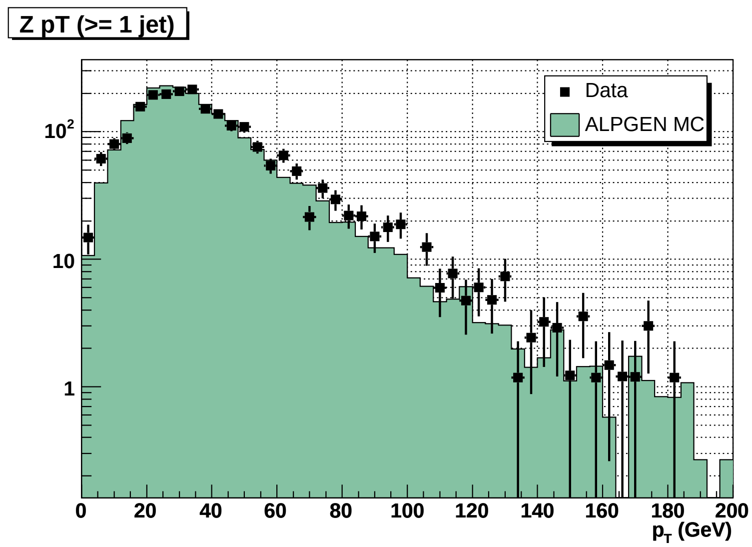

Figure 6: Comparison of Z p_T between data and ALPGEN $Z+ \geq 1$ jet MC. MC is normalized to the number of events in data.

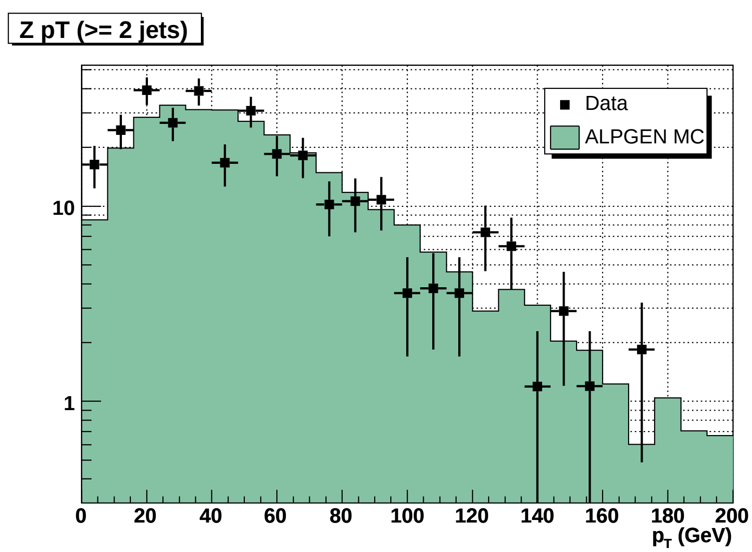

Figure 7: Comparison of Z p_T between data and ALPGEN $Z+ \geq 2$ jets MC. MC is normalized to the number of events in data.

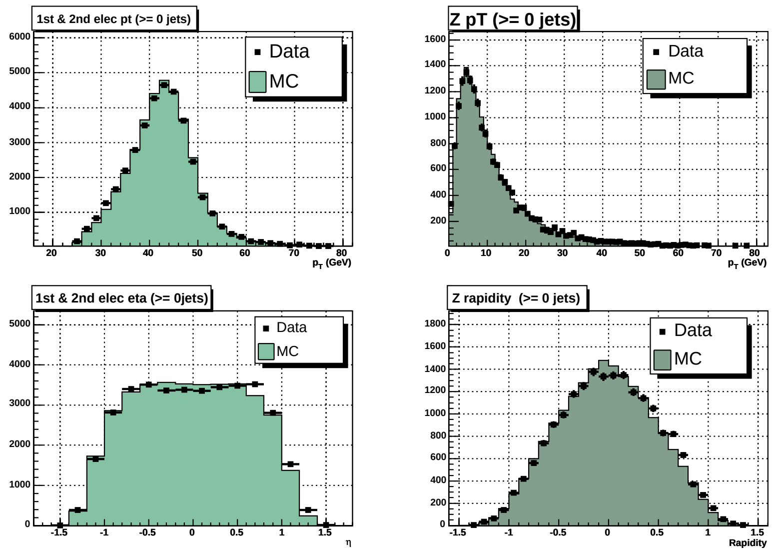

Figure 8: pT of both Z electrons (top left), physics η of both Z electrons (bottom left), Z p_T (top right), Z rapidity (bottom right) for the $Z/\gamma^* \to e^+e^-$ inclusive sample in data and MC (PYTHIA). The MC distribution is normalized to the number of events in data.

5.3 Z/γ^* $(\to e^+e^-) + \geq n$ Jet Comparisons

5.3.1 Z/γ^* $(\to e^+e^-)$ Inclusive Sample

In this section, basic kinematic distributions for electrons and Z candidates are compared after applying all corrections (Trigger, EM, Tracking, Z p_T - see Sections 6.1 and 7.1 for a description of the corrections). Figure 8 compares basic electron and Z kinematic distributions. Figure 9 compares the diem invariant mass distribution. The average Z mass is 91.02 GeV with a width of 4.03 GeV.

5.3.2 Z/γ^* $(\to e^+e^-) + \geq 1$ Jet Sample

Figure 10 shows comparisons of basic electron and Z distributions. Figure 11 shows a comparison of the diem invariant mass peak. Figures 12 and 13 show comparisons of basic kinematic distributions for jets.

5.3.3 Z/γ^* $(\to e^+e^-) + \geq 2$ Jet Sample

Figure 14 shows comparisons of basic electron and Z distributions. Figure 15 shows a comparison of the diem invariant mass peak and Figures 16, 17 and 18 show comparisons of basic kinematic distributions for jets.

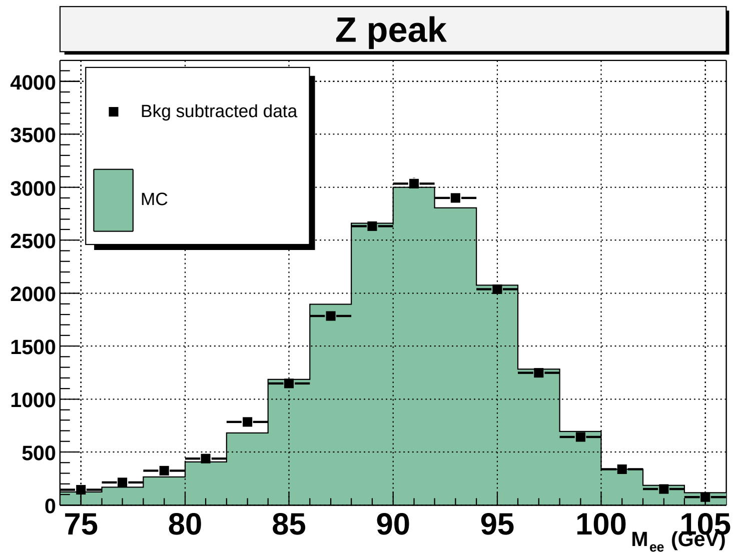

Figure 9: Diem invariant mass comparison for the $Z/\gamma^* \to e^+e^-$ inclusive sample in data and MC (PYTHIA). Data are background subtracted. The MC distribution is normalized to the number of events in data.

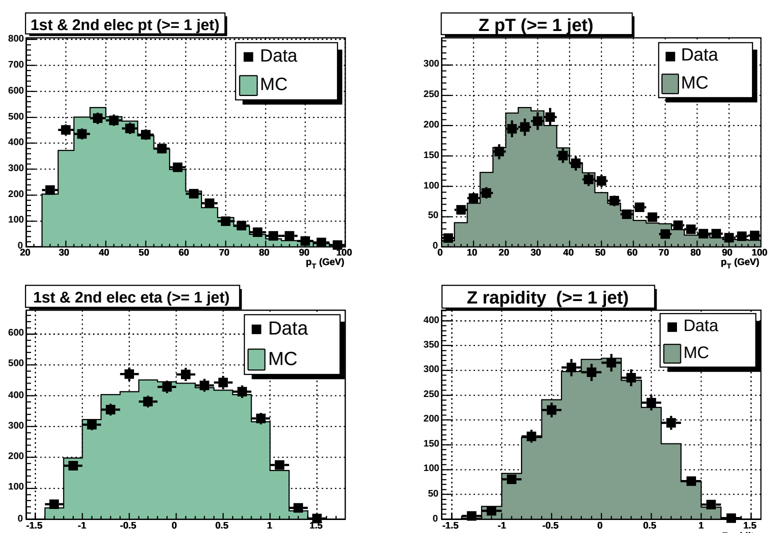

Figure 10: pT of both Z electrons (top left), physics η of both Z electrons (bottom left), Z p_T (top right), Z rapidity (bottom right) for the $Z/\gamma^* \to e^+e^- + \geq 1$ jet sample in data and MC (ALPGEN). The MC distributions are normalized to the number of events in data.

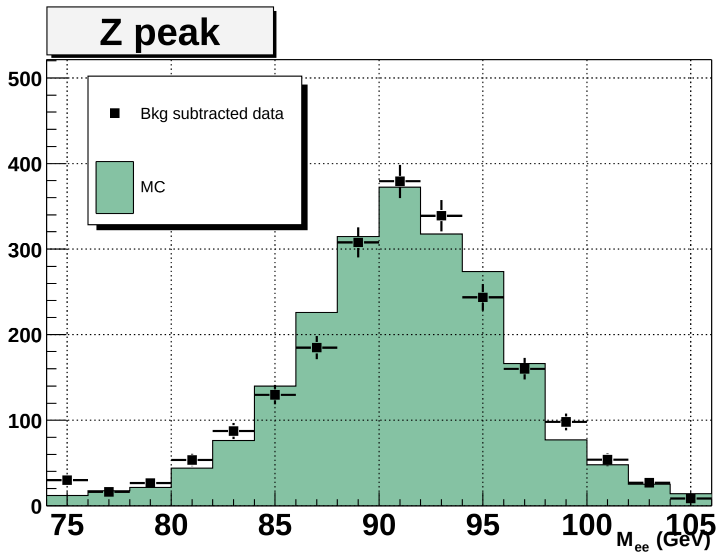

Figure 11: Diem invariant mass comparison for the $Z/\gamma^* \to e^+e^- + \geq 1$ jet sample in data and MC (ALPGEN). Data are background subtracted. The MC distribution is normalized to the number of events in data.

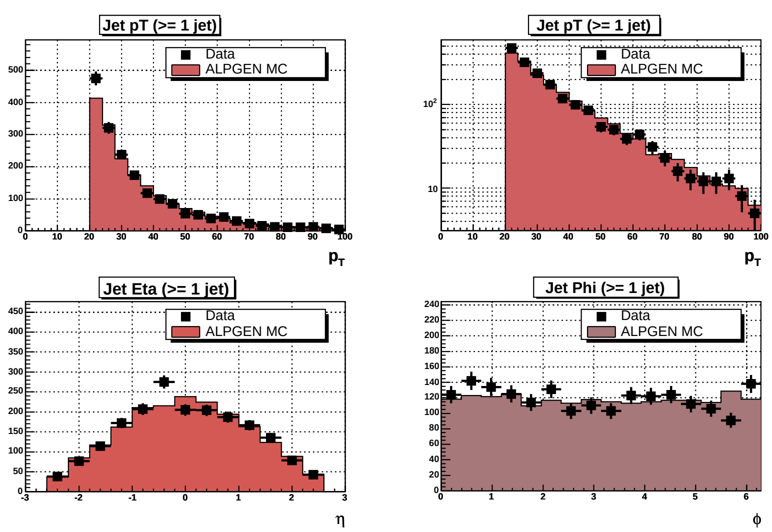

Figure 12: p_T (linear and logarithmic), physics η and physics Φ of all jets for the $Z/\gamma^* \to e^+e^- + \geq 1$ jet sample in data and MC (ALPGEN). The MC distributions are normalized to the number of events in data.

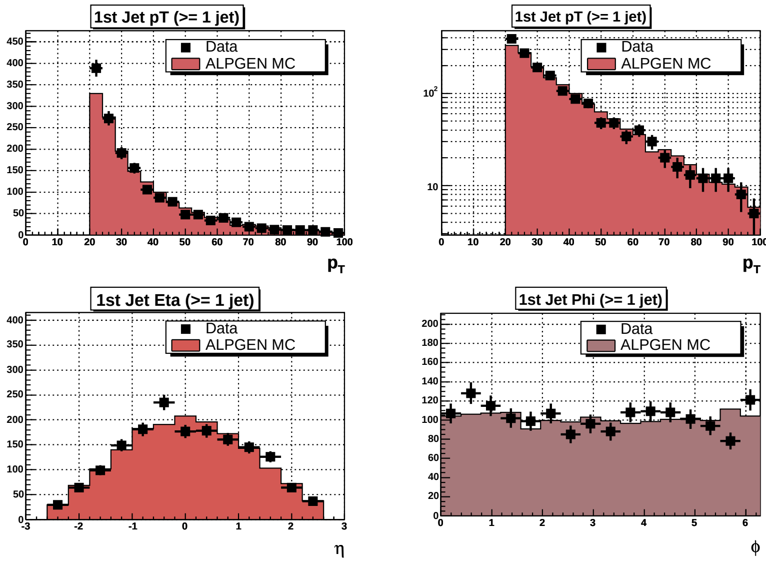

Figure 13: p_T (linear and logarithmic), physics η and physics Φ of the leading p_T jet for the $Z/\gamma^* \to e^+e^- + \geq 1$ jet sample in data and MC (ALPGEN). The MC distributions are normalized to the number of events in data.

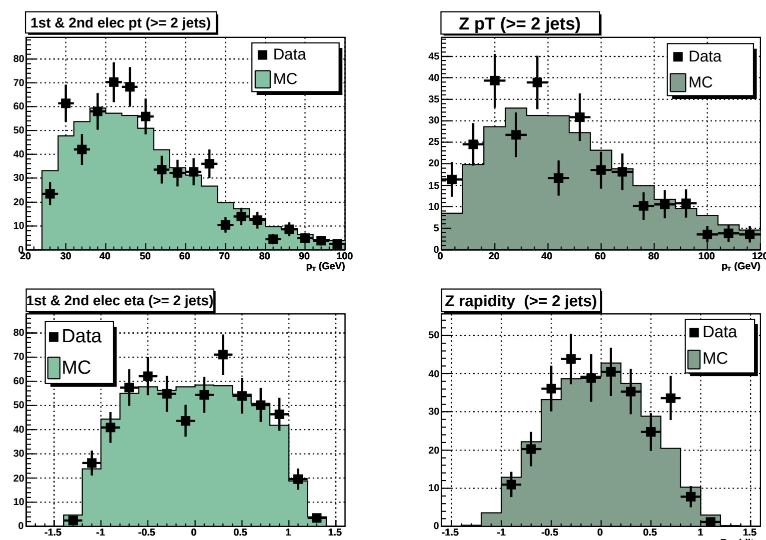

Figure 14: pT of both Z electrons (top left), physics η of both Z electrons (bottom left), Z p_T (top right), Z rapidity (bottom right) for the $Z/\gamma^* \to e^+e^- + \geq 2$ jet sample in data and MC (ALPGEN). The MC distributions are normalized to the number of events in data.

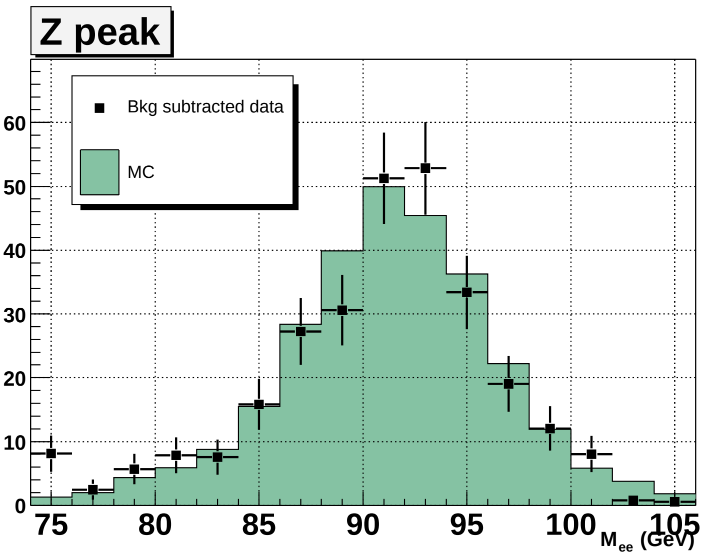

Figure 15: Diem invariant mass comparison for the $Z/\gamma^* \to e^+e^- + \geq 2$ jet sample in data and MC (ALPGEN). Data are background subtracted. The MC distribution is normalized to the number of events in data.

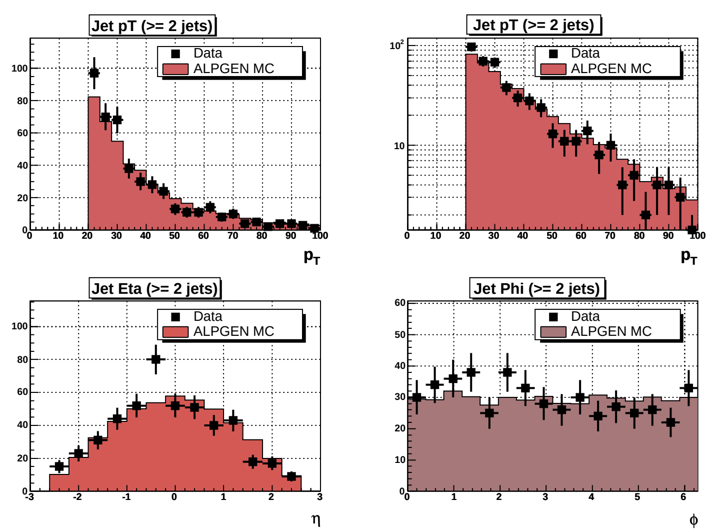

Figure 16: p_T (linear and logarithmic), physics η and physics Φ of all jets for the $Z/\gamma^* \to e^+e^- + \geq 2$ jet sample in data and MC (ALPGEN). The MC distributions are normalized to the number of events in data.

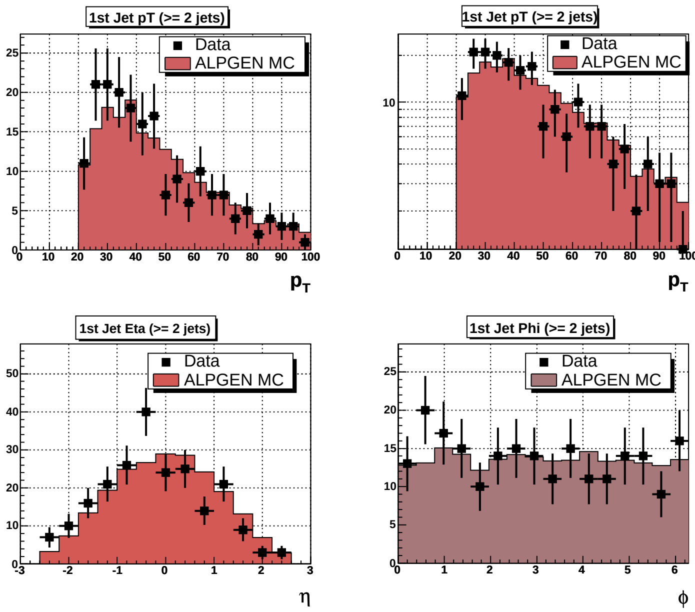

Figure 17: p_T (linear and logarithmic), physics η and physics Φ of the leading p_T jet for the $Z/\gamma^* \to e^+e^- + \geq 2$ jet sample in data and MC (ALPGEN). The MC distributions are normalized to the number of events in data.

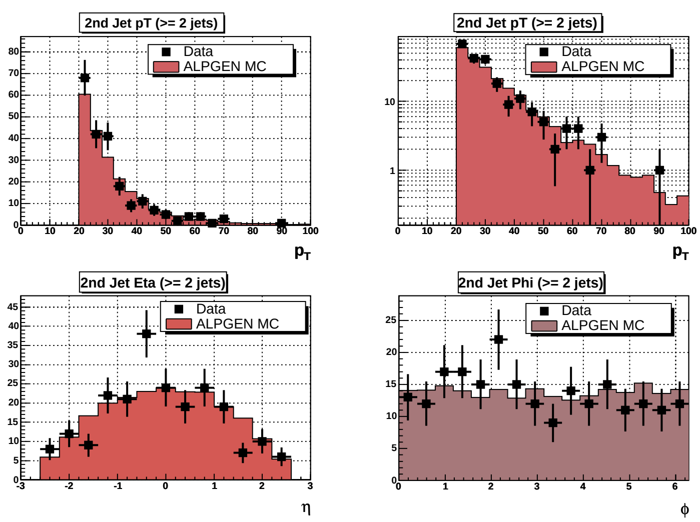

Figure 18: p_T (linear and logarithmic), physics η and physics Φ of the second leading p_T jet for the $Z/\gamma^* \to e^+e^- + \geq 2$ jet sample in data and MC (ALPGEN). The MC distributions are normalized to the number of events in data.

6 Measurement of the $Z/\gamma^*(\rightarrow e^+e^-)$ Inclusive Cross Section

The $Z/\gamma^*(\rightarrow e^+e^-)$ inclusive cross section is measured to provide a basic cross check for some of the techniques used in the final measurement of the $Z/\gamma^*(\rightarrow e^+e^-)+\geq n$ jet cross sections. In order to determine the inclusive cross section times branching fraction into electrons, the following equation is evaluated:

$$\sigma \times \mathrm{BR}(Z/\gamma^* \rightarrow e^+e^-) = \frac{N-B}{\mathcal{L} \times \varepsilon_{tot} \times A}, \tag{7}$$

where N and B are the total number of events and number of background events in the diem invariant mass range, respectively; $\mathcal{L}$ is the total integrated luminosity of the data sample (343 pb^{-1}); A is the *acceptance*, i.e. the efficiency of the kinematic and geometric electron cuts, the diem invariant mass cut and the primary vertex cut; and ε_{tot} is the total efficiency to identify e^+e^- pairs resulting from Z/γ^* decays. ε_{tot} can be further factorized according to:

$$\varepsilon_{tot} = \varepsilon_{trigger} \cdot \varepsilon_{EM} \cdot \varepsilon_{track}, \tag{8}$$

where $\varepsilon_{trigger}$ is the efficiency of the event to have at least one electron to pass all trigger levels, ε_{EM} is the efficiency of reconstructing two EM clusters which pass all electron ID cuts, and ε_{track} is the efficiency of requiring at least one EM cluster to match with a track. Practically, all efficiencies are applied as corrections to the diem invariant mass distribution.

The primary source of background to Z/γ^* decays is from QCD multi-jet production in which the jets have a large electromagnetic component or are mismeasured in such a way that the jets pass the electron selection criteria. The shape of the QCD background in the diem invariant mass distribution follows an exponential form. This is determined by examining the diem invariant mass distribution of EM object pairs that were selected by applying "anti-electron cuts" to assure that two jets with high electromagnetic energy content in the shower are selected:

- All criteria that are applied to loose electron candidates as described in Section 4.2 except for the H-Matrix cut.
- H-Matrix(7) > 35
- Two of these objects per event.

Additional background contributions due to $W \rightarrow e\nu$, $Z \rightarrow \tau\tau$, and $t\bar{t} \rightarrow l\nu bl\nu b$ processes were estimated by passing the respective MC samples through the event selection. The number of surviving background candidate events was then normalized with respect to the luminosity of the data sample. The overall background contribution due to these additional physics processes was found to be small (see Section 6.2).

The goal is to measure the cross section for diem pairs where both γ^* (*Drell-Yan*) and Z boson intermediate states contribute. Contributions from pure Z

boson decays will show up as a peak around the Z mass at ≈ 91 GeV in the diem invariant mass distribution. The Drell-Yan component follows an exponential distribution.

The following section describes the determination of the efficiencies (trigger, EM reconstruction and identification, EM-Track match) and acceptance.

6.1 Efficiencies

6.1.1 Trigger Efficiency

The combined trigger efficiency per electron is determined with a *tag-and-probe method* using Z candidate events with invariant mass between 70 and 110 GeV. For this method, both Z candidate electrons are considered as possible "tags". An electron becomes a "tag" if it passes trigger requirements for at least one unprescaled trigger in the trigger combination. To pass the requirements of a trigger, an electron must have a matching trigger object at each level which passes all cuts for the corresponding trigger. Both the tag and probe electrons must satisfy the following requirements:

- $p_T > 20$ GeV
- EM Fraction > 0.9
- Isolation < 0.15
- H-Matrix(7) < 12
- Track match with $P(\chi^2) > 0.01$.

The probe electron must have matching trigger objects at L1, L2 and L3 within $\Delta R = \sqrt{\Delta\eta^2 + \Delta\phi^2}$ of 0.4.

Trigger efficiencies are parameterized versus EM object p_T and derived separately for pre-v12 and v12 data. In cases where the L2 subsystem was not operative (all runs before 169,524), only L1 and L3 trigger objects were used. Figure 19 shows the parameterized trigger efficiencies for both datasets.

The average trigger efficiencies per electron for the pre-v12 and v12 datasets are (with statistical uncertainties):

- $\varepsilon^{electron}_{pre-v12}(\text{Trigger}) = 94.6\% \pm 0.3\%$
- $\varepsilon^{electron}_{v12}(\text{Trigger}) = 98.2\% \pm 0.1\%$.

The event trigger efficiency is calculated in the following way:

- In a given event the trigger efficiency curves are used to determine the trigger efficiencies ε_1 and ε_2 for the two EM objects (based on their p_T).
- To calculate the event based trigger efficiency, all permutations for the two EM objects to fire a trigger are taken into account:

$$\varepsilon^{event}_{trigger} = \varepsilon_1 \cdot (1 - \varepsilon_2) + \varepsilon_2 \cdot (1 - \varepsilon_1) + \varepsilon_1 \cdot \varepsilon_2 = \varepsilon_1 + \varepsilon_2 - \varepsilon_1 \cdot \varepsilon_2. \quad (9)$$

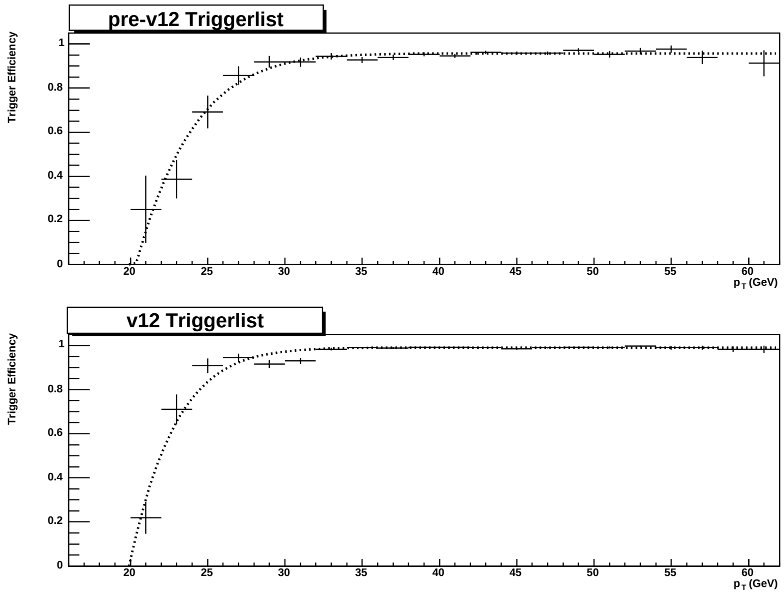

Figure 19: Trigger efficiencies for pre-v12 (top) and v12 (bottom) datasets vs EM object p_T
.

6.1.2 EM Reconstruction and Identification Efficiency

To determine EM efficiencies, a tag and probe method is used. The tag leg consists of an electron candidate, and the probe leg consists of a track. The tag electron has to pass all the loose electron selection cuts, have a matched track and satisfy trigger requirements for the event. Both tag and probe tracks have to satisfy the following selection criteria [17]:

- Stereo track[7]
- 25 GeV $< p_T <$ 80 GeV
- χ^2 probability for best track < 8 (using the spatial distance in η and Φ and the E/p ratio)
- Distance of closest approach between track and beam position in the R-Φ plane < 0.3 cm
- Δz_{vertex} of the two tracks < 4 cm
- $|\eta_{detector}| < 1.1$.

Tag electron selection criteria:

[7]Requiring hits in stereo layers of the tracking system.

- ID = 10 or ± 11
- EMFraction > 0.9
- Isolation < 0.15
- H-Matrix(7) < 12
- $p_T > 25$ GeV
- $|\eta_{detector}| < 1.1$
- No fiducial restrictions in ϕ.
- Matched with tag track within $\Delta R = \sqrt{\Delta\eta^2 + \Delta\phi^2} = \sqrt{0.1^2 + 0.1^2} = 0.14$.
- Must have fired the trigger.

Possible background contamination is reduced by requiring that tag- and probe-tracks have opposite signs, and by imposing a cut on the missing transverse energy of the event (missing $E_T < 15$ GeV). The following lists additional requirements:

- $|PVZ| < 60$ cm
- Tag-electron-and-probe-track invariant mass cut: 70 GeV $< M_{ee} <$ 110 GeV.

Once an event is found which satisfies all of the above requirements, a denominator histogram is filled. If a reconstructed EM cluster is found nearby the probe-track ($\Delta R = \sqrt{\Delta\eta^2 + \Delta\phi^2} = \sqrt{0.1^2 + 0.1^2} = 0.14$[8]) which passes the EMID cuts (HMx, EMF, Iso), the respective numerator histogram is filled.

Figures 20 and 21 show the EM efficiencies for data and MC in a one-dimensional parameterization versus probe track Φ and p_T. Note that the central calorimeter has narrow uninstrumented regions between the azimuthal module boundaries (*phi cracks*). An EM object entering the calorimeter near these boundaries can lose a portion of its energy in these cracks, which results in decreased EM efficiencies for these regions.

The average EM reco and ID efficiencies are derived by dividing the tag-electron-and-probe-track-matched-EM diem invariant mass histograms with the tag-electron-and-probe-track diem invariant mass histograms. The diem invariant mass distributions have background contamination. We estimate the background in the signal region by using the sidebands of the diem invariant mass distributions.

The average EM reco and ID efficiencies in data and MC are (with statistical uncertainties):

[8]Tracks are extrapolated to the third EM layer of the calorimeter using detector coordinates.

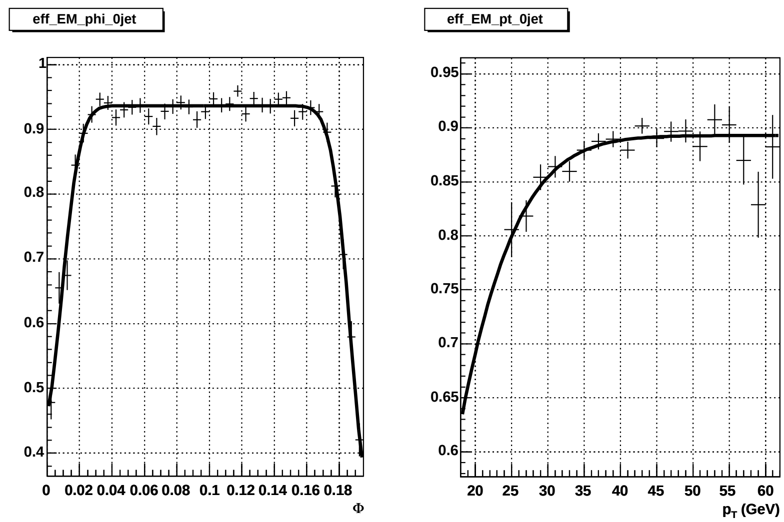

Figure 20: EM efficiencies versus probe track Φ and p_T in data. The Φ distribution shows the modulus(Φ, $\frac{2\pi}{32}$) distribution to illustrate the effect of the calorimeter Φ-module boundaries.

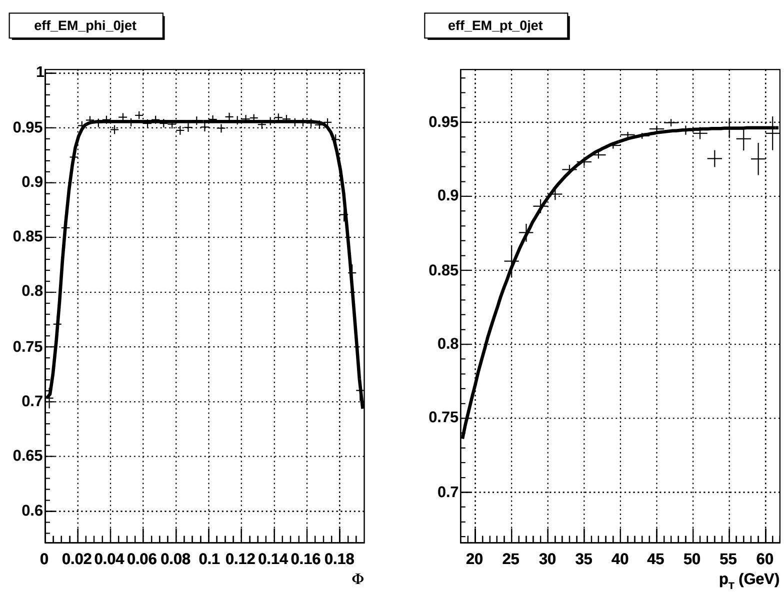

Figure 21: EM efficiencies versus probe track Φ and p_T in MC. The Φ distribution shows the modulus(Φ, $\frac{2\pi}{32}$) distribution to illustrate the effect of the calorimeter Φ-module boundaries.

- $\varepsilon^{electron}_{data}(\text{EM}) = 88.9\% \pm 0.3\%$
- $\varepsilon^{electron}_{MC}(\text{EM}) = 93.1\% \pm 0.1\%$.

The sideband background subtraction cannot be applied in the case of parameterized efficiencies, since no diem invariant mass distributions are used. The level of background contamination is examined by deriving the average efficiency in data without the sideband background subtraction. The result is within 1% of the sideband subtracted value: 88.2% ± 0.2%.

EM event efficiencies are calculated in the following way:

- In a given event two-dimensional efficiency curves are used (versus p_T and Φ) to estimate the EM efficiencies ε_1 and ε_2 for the two EM objects (based on their p_T and Φ).
- To calculate the event based EM efficiency, the product of ε_1 and ε_2 is taken:
$$\varepsilon_{EM} = \varepsilon_1 \cdot \varepsilon_2. \tag{10}$$

6.1.3 EM-Track Match Efficiency

Average track finding and matching[9] efficiencies are derived using diem invariant mass distributions (Figures 22 to 25).

Using a convolution of a Gaussian and Breit-Wigner fit for the Z peak and an exponential shape to describe the QCD and Drell-Yan contributions, the number of events under the Z peak is extracted from the four diem invariant mass distributions: $N_{1trk}(data)$, $N_{2trk}(data)$, $N_{1trk}(MC)$ and $N_{2trk}(MC)$. $N_{1trk}(data)$ and $N_{1trk}(MC)$ are the number of Z candidates with at least one track match in data and MC; $N_{2trk}(data)$ and $N_{2trk}(MC)$ are the number of Z candidates with exactly two track matches in data and MC. These numbers are used to estimate the average track finding and track matching efficiencies per electron in data and MC:

$$\varepsilon^{electron}_{data}(\text{Tracking}) = \frac{2 \cdot N_{2trk}(data)}{N_{2trk}(data) + N_{1trk}(data)} = 77.1\% \pm 0.3\% \tag{11}$$

$$\varepsilon^{electron}_{MC}(\text{Tracking}) = \frac{2 \cdot N_{2trk}(MC)}{N_{2trk}(MC) + N_{1trk}(MC)} = 87.8\% \pm 0.03\%. \tag{12}$$

The event based tracking efficiency is calculated in the following way:

- In each event the average electron tracking efficiency $\varepsilon^{electron}_{tracking}$ is used (Equations 11 and 12).
- To calculate the event based tracking efficiency, all permutations for one or two track matched electrons are taken into account:
$$\varepsilon^{event}_{tracking} = 2 \cdot \varepsilon^{electron}_{tracking}(1 - \varepsilon^{electron}_{tracking}) + {\varepsilon^{electron}_{tracking}}^2 = 2 \cdot \varepsilon^{electron}_{tracking} - {\varepsilon^{electron}_{tracking}}^2 \tag{13}$$

[9] $P(\chi^2) > 0.01$, with χ^2 probability for best track using the spatial distance in η and Φ and the E/p ratio.

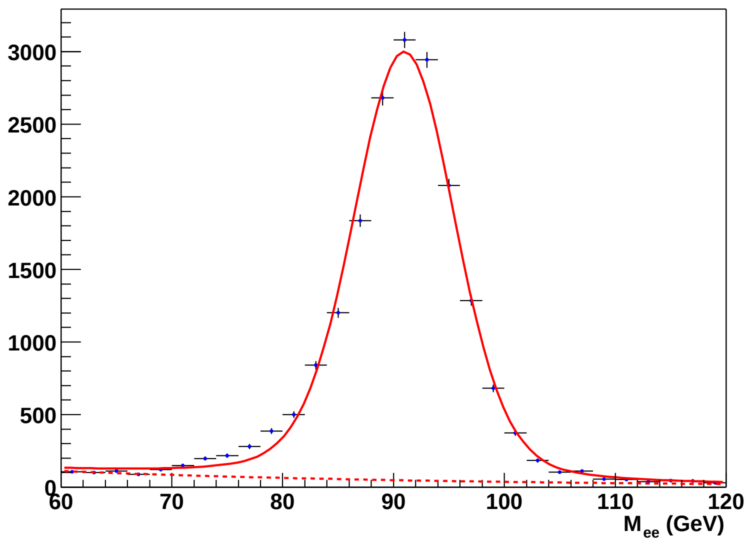

Figure 22: Invariant mass with at least one track-matched electron (data).

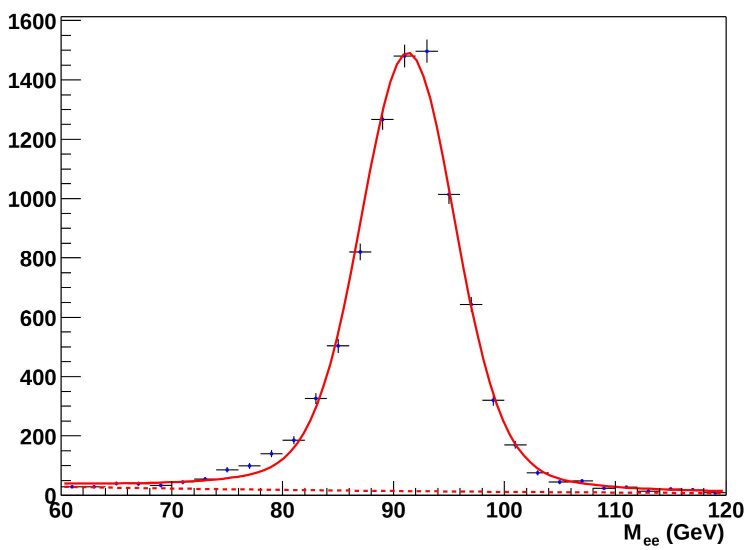

Figure 23: Invariant mass with two track-matched electrons (data).

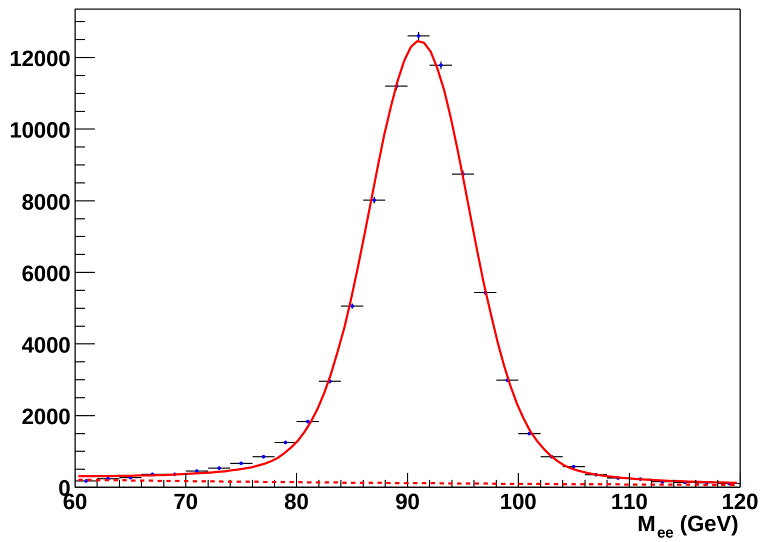

Figure 24: Invariant mass with at least one track-matched electron (MC).

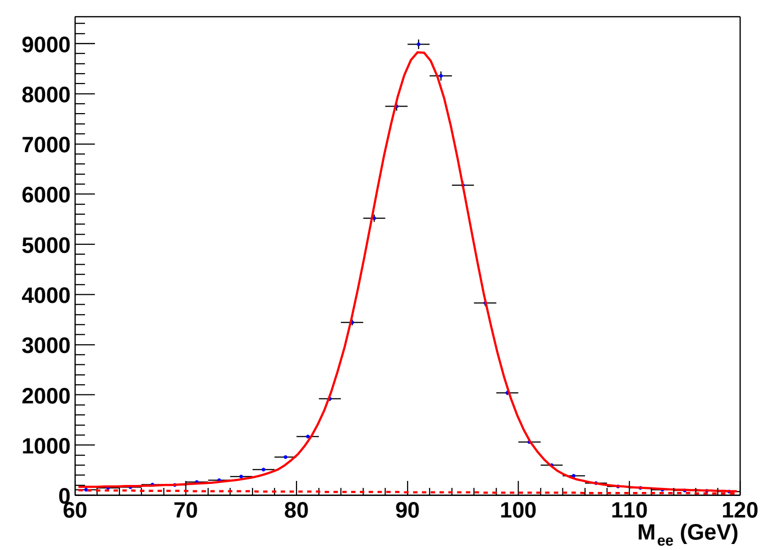

Figure 25: Invariant mass with two track-matched electrons (MC).

6.1.4 Acceptance

The $Z/\gamma^* \rightarrow e^+e^-$ PYTHIA MC sample with detector simulation is used to estimate the acceptance for the fiducial and kinematic cuts. The acceptance numerator counts the number of events satisfying the following requirements at the detector reconstructed level:

- Primary vertex cut: $|PVZ| < 60$ cm
- Electron cuts: $p_T > 25$ GeV and $|\eta_{det}| < 1.1$
- Diem invariant mass cut: 75 GeV $< M_{ee} <$ 105 GeV.

The acceptance denominator counts the number of events with generated Z/γ^* particles that are within the diem invariant mass window.

Since the acceptance calculation involves two reconstructed electrons, a corrective weight is applied to the reconstructed event. Based on the p_T and Φ values of the two electrons, the reconstruction efficiencies are estimated to be $\approx 98\%$. The product of the inverse of those reconstruction efficiencies yields a corrective weight. The Z p_T correction factor is also applied (see Section 5.2) as an additional weight in both the numerator and denominator of the acceptance.

The acceptance with statistical uncertainty for inclusive $Z/\gamma^* \rightarrow e^+e^-$ is estimated to be:

$$A(Z/\gamma^* \rightarrow e^+e^- + X) = 21.4\% \pm 0.1\%. \tag{14}$$

6.2 Cross Section Calculation

After applying all corrections, the number of corrected signal events is determined from the diem invariant mass distribution (Figure 26). A convolution of a Gaussian and Breit-Wigner shape is fitted to the Z peak. An exponential shape is used to describe the QCD and Drell-Yan contributions.

Since the Drell-Yan component is part of the signal, the QCD component needs to be disentangled from the Drell-Yan component. Using the inclusive $Z/\gamma^* \rightarrow e^+e^-$ PYTHIA MC sample, the percentage of Drell-Yan events in $Z/\gamma^* \rightarrow e^+e^-$ decays is estimated by fitting a Gaussian and Breit-Wigner shape to the Z component and an exponential shape to the Drell-Yan component. 2.06% of the events in the inclusive $Z/\gamma^* \rightarrow e^+e^-$ sample are due to Drell-Yan.

Based on these fits, the number of signal events from direct Z boson and Drell-Yan decays is extracted, as well as the number of QCD background events in the diem invariant mass signal window (75 GeV $< M_{ee} <$ 105 GeV) [10]. We also quote the small contributions from additional physics backgrounds:

- Number of signal events from Z Boson and Drell-Yan decays = 18223.5
- Number of QCD background events = 407.5

[10] The number of signal events is derived by counting all entries for a particular M_{ee} bin and subtracting from it the number of entries from the background fit.

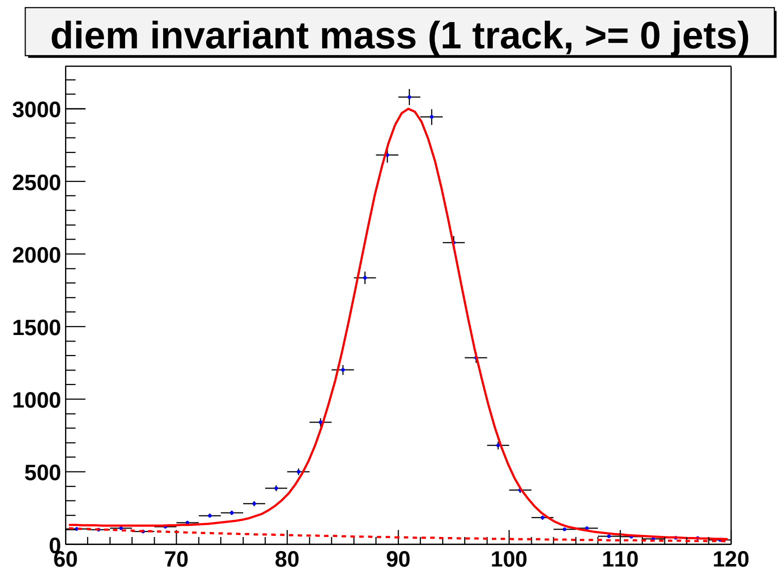

Figure 26: Diem invariant mass distribution for $Z/\gamma^* \to e^+e^- + X$ (Mean = 91.02 GeV $\pm$ 0.04 GeV, Width 4.03 GeV $\pm$ 0.04 GeV).

- Number of $W \to e\nu$ background events = 32.0
- Number of $Z \to \tau\tau$ background events = 6.2
- Number of $t\bar{t} \to l\nu bl\nu b$ background events = 2.1

Based on the integrated luminosity (343 pb^{-1}) and the acceptance (21.4%), the inclusive Z/γ^* production cross section times branching fraction into electrons is calculated:

$$\sigma \times \text{BR}(Z/\gamma^* \to e^+e^-) = \frac{N - B}{\mathcal{L} \times A} = 248.4 \ \pm 2.5(\text{stat}) \text{ pb.} \tag{15}$$

In order to check the procedure that leads to the cross section measurement, a MC closure test was performed. The number of signal events, acceptance, and luminosity were evaluated in a PYTHIA MC sample. The calculated MC cross section (179 pb) was compared to the PYTHIA cross section that was used to generate the MC sample (183 pb). The calculated MC cross section was in good agreement with the MC input cross section.

6.3 Comparison to Other Measurements

Using the inclusive PYTHIA MC sample, a correction factor is derived to estimate the inclusive Z/γ^* cross section in a different diem invariant mass range

(66 GeV $< M_{ee} <$ 116 GeV) [11]. The number of Z/γ^* candidates is counted at the particle level in the new diem invariant mass range. A ratio is taken which yields the correction to account for the change in the diem invariant mass range [18].

The result of 257.4 pb is compared with the CDF measurement [19] for the inclusive Z/γ^* cross section (66 GeV $< M_{ee} <$ 116 GeV) of 255.8 $\pm$ 3.9(stat) pb. Both results are in good agreement.

7 Measurement of the $\mathbf{Z/\gamma^*(\rightarrow e^+e^-)+\geq n}$ Jet Cross Sections

This section outlines the procedure to measure the $Z/\gamma^*(\rightarrow e^+e^-)$ production cross section for different inclusive jet multiplicities. For each jet multiplicity the number of signal events is determined from the diem invariant mass histograms in the range of 75-105 GeV. All efficiencies are examined for jet multiplicity dependence and applied to the diem invariant mass distributions as corrections. The cross sections as a function of jet multiplicity are also corrected for jet reconstruction and identification efficiencies, and for event migration due to the finite jet energy resolution of the detector (*unsmearing*).

The following sections outline the determination of all efficiencies and acceptances, as well as the unsmearing procedure and the cross section evaluation.

7.1 Efficiencies vs Jet Multiplicity

In the following sections the PYTHIA MC sample is used to derive corrections for the inclusive sample, while ALPGEN MC samples are used for the n-jet corrections.

7.1.1 Trigger Efficiency

The electron trigger efficiency as a function of jet multiplicity is measured (Figure 27). No significant variation in the trigger efficiencies is observed as jet activity increases[12]. Therefore, the same trigger corrections as for the inclusive sample are applied to all jet multiplicity bins (see Section 6.1.1). Table 7 summarizes electron trigger efficiencies for the pre-v12 and v12 datasets for different inclusive jet multiplicities. A systematic uncertainty of $\pm$5% for the object based trigger efficiencies is assigned for all jet multiplicities.

7.1.2 EM Reconstruction and Identification Efficiency

Averaged single-EM efficiencies are derived using the procedure outlined in Section 6.1.2 in data and MC for different jet multiplicities (Figure 28). The same

[11] The MC sample used a generator cut of $|\eta_Z| < 4.2$. Although no restriction in η_Z would have been preferable, the impact on the final results is believed to be negligible.

[12] Any possible decrease of the object based trigger efficiency versus jet multiplicity for the v12 dataset would yield a negligible contribution to the overall event based trigger efficiency.

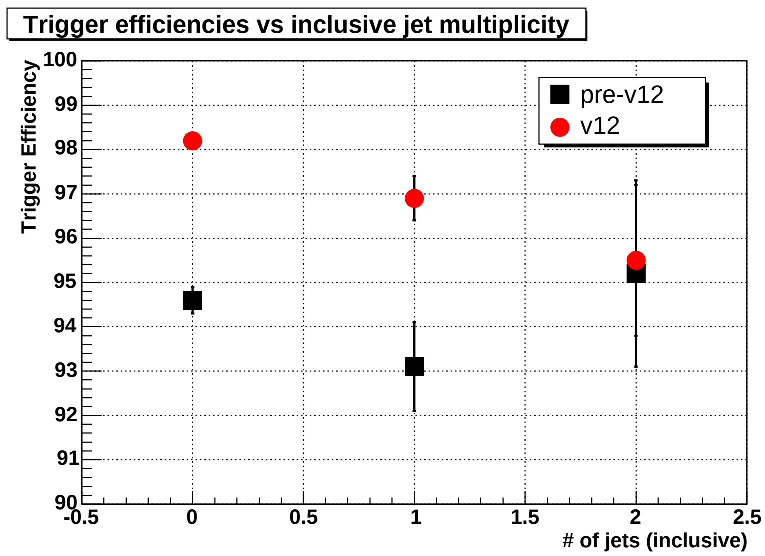

Figure 27: Average object based trigger efficiencies in data versus inclusive jet multiplicity.

Jet multiplicity	pre-v12	v12
≥ 0	$94.6\% \pm 0.3\%$	$98.2\% \pm 0.1\%$
≥ 1	$93.1\% \pm 1.0\%$	$96.9\% \pm 0.5\%$
≥ 2	$95.2\% \pm 2.1\%$	$95.5\% \pm 1.7\%$

Table 7: Object based trigger efficiencies with statistical uncertainties for the pre-v12 and v12 datasets for different inclusive jet multiplicities.

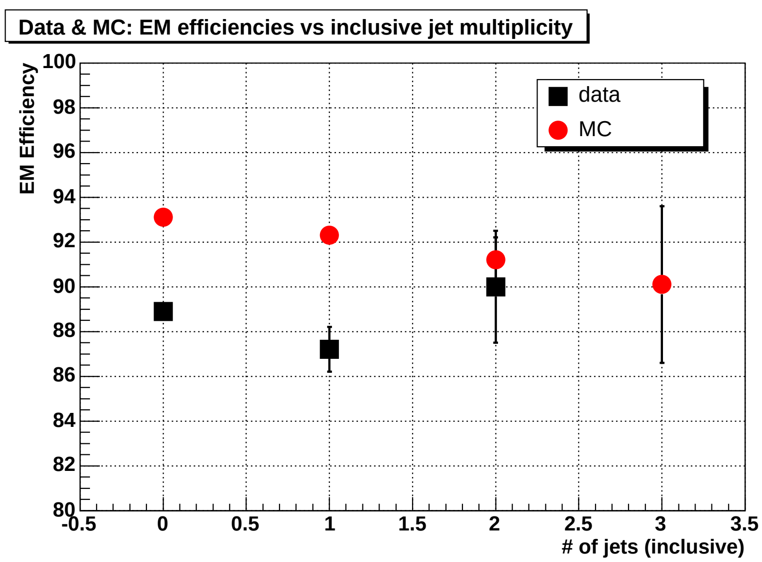

Figure 28: Average object based EM reco and ID efficiencies in data and MC versus inclusive jet multiplicity. There was not enough statistics available to estimate the EM efficiency in data for ≥ 3 jets.

EM corrections as for the inclusive sample are applied to each jet multiplicity sample. Residual inefficiencies due to additional jet activity are examined (Figure 28). Table 8 summarizes the EM reco and ID efficiencies in data and MC for different jet multiplicities.

No significant change of the average object based efficiencies with respect to jet multiplicity is observed in data. Therefore, no residual correction is applied. From the fluctuations of the single-EM reconstruction and ID efficiencies, a systematic uncertainty of $\pm 3\%$ is assigned for all jet multiplicities.

Based on the efficiency drop in MC a corrective weight is applied to each jet multiplicity. The value for the weight is derived by taking the ratio of the EM efficiency for the inclusive sample and the average of the EM efficiencies for the

Jet multiplicity	data	MC
≥ 0	$88.9\% \pm 0.3\%$	$93.1\% \pm 0.1\%$
≥ 1	$87.2\% \pm 1.0\%$	$92.3\% \pm 0.3\%$
≥ 2	$90.0\% \pm 2.5\%$	$91.2\% \pm 1.0\%$
≥ 3	(n/a)	$90.1\% \pm 3.5\%$

Table 8: Object based EM reco and ID efficiencies with statistical uncertainties in data and MC for different inclusive jet multiplicities. There was not enough statistics available to estimate the EM efficiency in data for ≥ 3 jets.

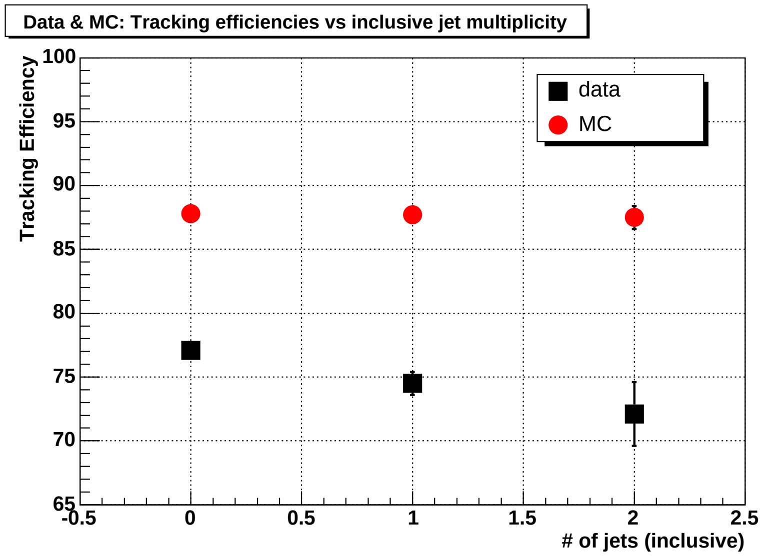

Figure 29: Average object based tracking efficiencies in data and MC versus inclusive jet multiplicity.

Jet multiplicity	data	MC
≥ 0	77.1% $\pm$ 0.3%	87.8% $\pm$ 0.03%
≥ 1	74.5% $\pm$ 0.9%	87.7% $\pm$ 0.3%
≥ 2	72.1% $\pm$ 2.5%	87.5% $\pm$ 0.9%

Table 9: Object based tracking efficiencies with statistical uncertainties in data and MC for different inclusive jet multiplicities.

1-jet, 2-jet and 3-jet samples.

7.1.3 EM-Track Match Efficiency

Figure 29 and Table 9 show the average object based tracking efficiencies for different jet multiplicities. In MC, no efficiency variations are observed. Therefore, the value from the inclusive sample is used to correct for tracking inefficiencies for all jet multiplicities. In data, the inclusive value is used for the inclusive sample, the 1-jet value is used for the 1-jet multiplicity and the 2-jet value is used for all multiplicities of 2 and above.

Table 10 lists the systematic uncertainties for the data efficiencies. For the 1-jet and 2-jet samples, the respective statistical uncertainties are used as systematics. For the 3-, 4-, and 5-jet samples, the systematic uncertainty is estimated from the statistical uncertainty of the 2-jet bin added in quadrature with the difference between the 2-jet efficiency value, and a linear fit to the 0-,

Jet multiplicity	Data Efficiency	Systematic Uncertainty
≥ 0	77.1%	$\pm$ 0.3%
≥ 1	74.5%	$\pm$ 0.9%
≥ 2	72.1%	$\pm$ 2.5%
≥ 3	72.1%	$\pm$ 3.5%
≥ 4	72.1%	$\pm$ 5.6%
≥ 5	72.1%	$\pm$ 7.9%

Table 10: Object based tracking efficiencies with systematic uncertainties.

1-, and 2-jet bins extrapolated to the 3-, 4-, and 5-jet bins.

7.1.4 Acceptance

ALPGEN MC samples are used to estimate the kinematic and geometric acceptances for different jet multiplicities[13]. The numerator for the n-jet acceptance contains the number of events satisfying the following requirements:

- Primary vertex cut: $|PVZ| < 60$ cm
- Electron cuts: $p_T > 25$ GeV and $|\eta_{det}| < 1.1$
- Diem invariant mass cut: 75 GeV $< M_{ee} <$ 105 GeV
- Particle level jet cut: n jets with $p_T > 20$ GeV and $|\eta| < 2.5$.

The denominator for the n-jet acceptance contains the number of events satisfying the following requirements:

- MC generator diem invariant mass cut: 75 GeV $< M_{ee} <$ 105 GeV
- Particle level jet cut: n jets with $p_T > 20$ GeV and $|\eta| < 2.5$.

No additional Z p_T correction is needed since the Z p_T distributions between data and ALPGEN MC agree reasonably well (see Section 5.2). Table 11 summarizes the acceptances for different jet multiplicities. On average, higher jet multiplicities lead to higher Z p_T, since the Z boson recoils against the jet(s) in the event. This in turn leads to electrons coming from Z decays that are more likely to pass the acceptance requirements. Therefore, as jet multiplicities increase, acceptances increase as well.

7.1.5 Jet Reconstruction and Identification Efficiency

The jet reco/ID efficiency was estimated using a tuned MC sample according to the following procedure [20]:

[13] The Z+3 jet sample is used for jet multiplicities of 3, 4, and 5.

Jet multiplicity	Acceptance
≥ 0	$21.4\% \pm 0.1\%$
≥ 1	$25.1\% \pm 0.2\%$
≥ 2	$25.4\% \pm 0.2\%$
≥ 3	$27.4\% \pm 0.3\%$
≥ 4	$28.5\% \pm 0.7\%$
≥ 5	$30.3\% \pm 1.9\%$

Table 11: Acceptances with statistical uncertainties for different jet multiplicities.

- A scaling factor is derived based on the "Z p_T balance" method. This method selects events with Z candidates and probes for a recoiling jet opposite in Φ. The "efficiency" of finding a recoiling jet can be measured as a function of the Z p_T in data and MC (Figures 30 and 31).
- The ratio of the Z p_T "efficiency" in data and MC yields a scaling factor (Figure 32).
- The scaling factor is applied to the MC sample to tune it to match the data distributions.
- The tuned MC is used to measure the "straight" jet reco/ID efficiency by matching particle level jets with calorimeter jets within a search cone of ΔR = 0.4.
- The efficiency is parameterized versus particle jet p_T. The p_T values of the particle jets are smeared with the data energy resolutions (see Section 3.1).

Figures 33 and 34 show the MC and data jet reconstruction efficiencies for different regions in the calorimeter.

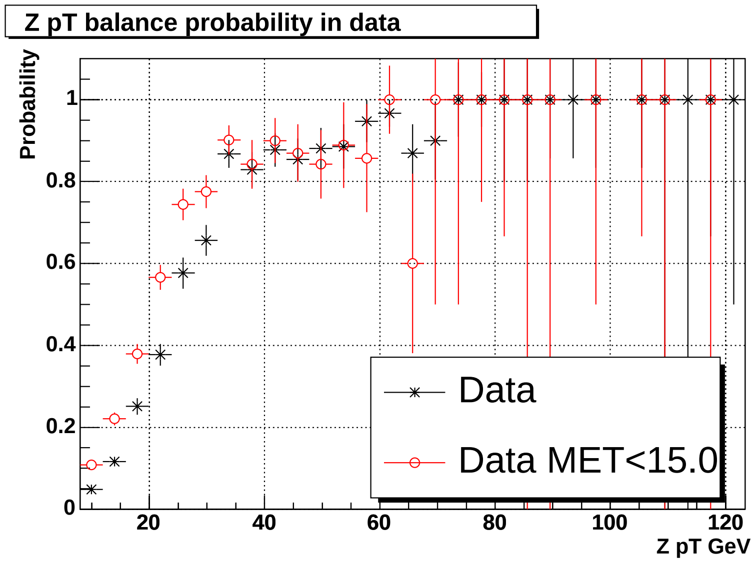

Figure 30: "Efficiency" of finding a recoiling jet as a function of Z p_T in data.

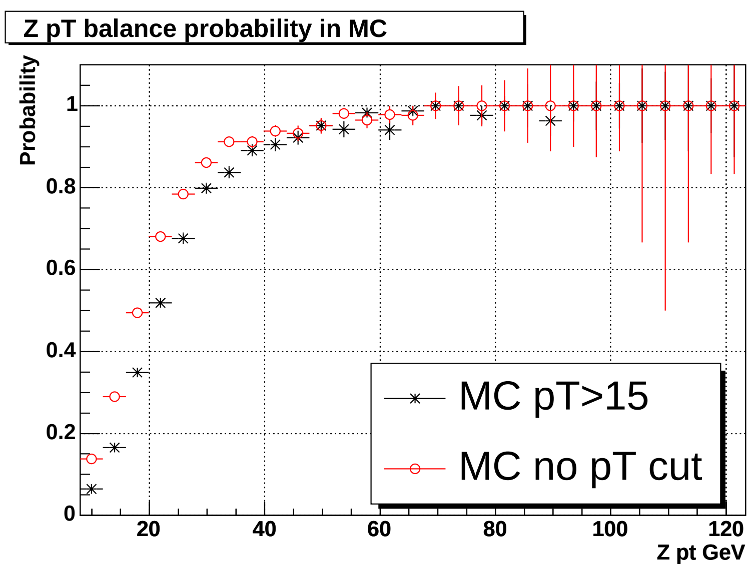

Figure 31: "Efficiency" of finding a recoiling jet as a function of Z p_T in MC.

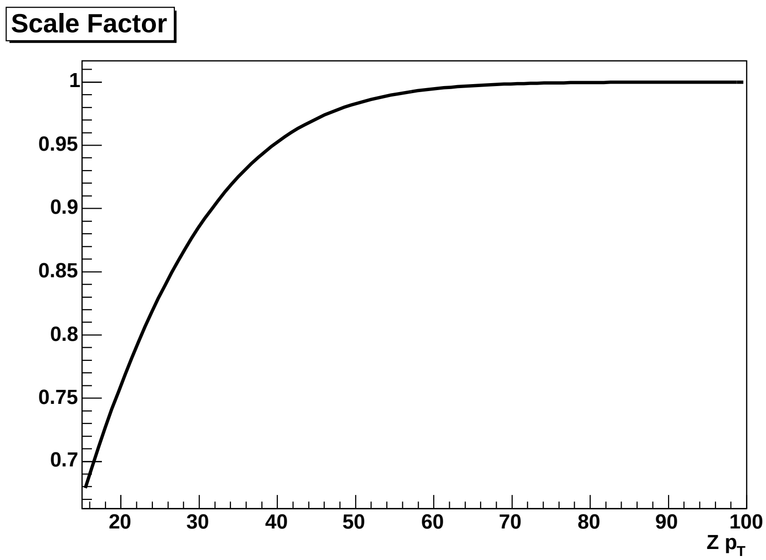

Figure 32: Data/MC scale factor as a function of Zp_T.

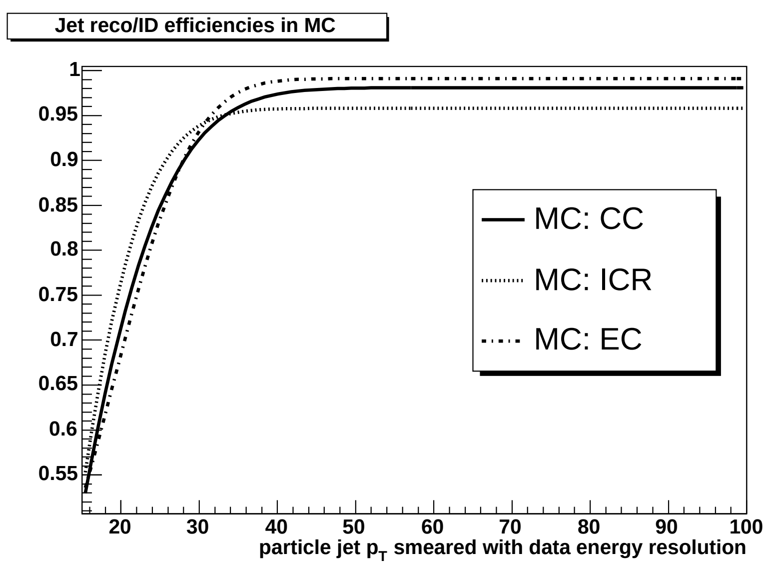

Figure 33: Jet reco/ID efficiencies in MC. CC $= -0.7 < |\eta_{det}| < 0.7$, ICR $= 0.7 < |\eta_{det}| < 1.5$, EC $= 1.5 < |\eta_{det}| < 2.5$.

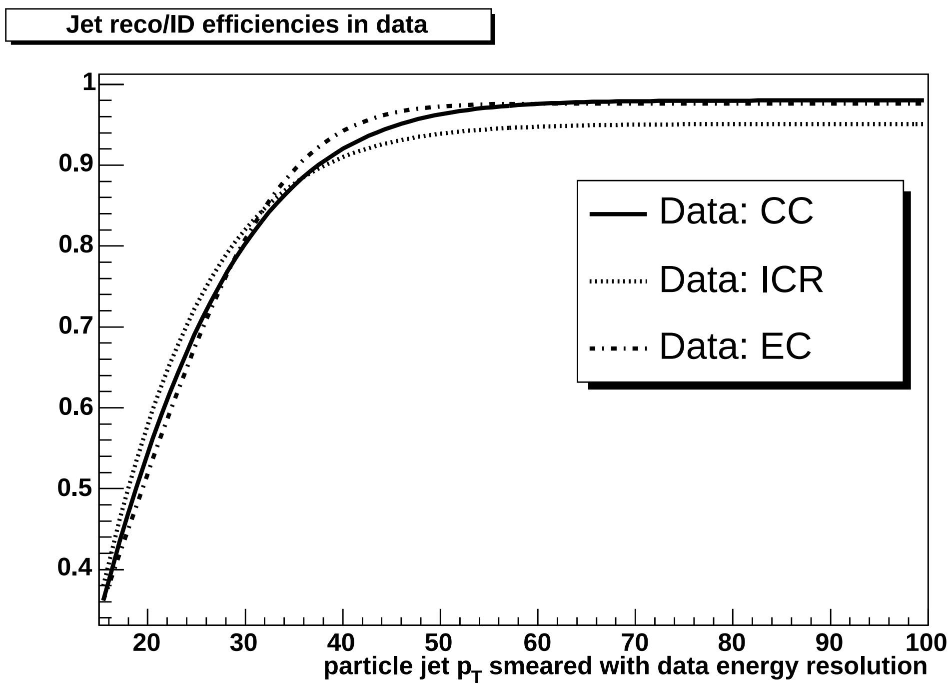

Figure 34: Jet reco/ID efficiencies in data. CC = $-0.7 < |\eta_{det}| < 0.7$, ICR = $0.7 < |\eta_{det}| < 1.5$, EC = $1.5 < |\eta_{det}| < 2.5$.

7.2 Cross Section Calculation

7.2.1 Unsmearing

In order to determine particle level cross sections, we correct the measured data jet multiplicities for event migration due to the finite jet energy resolution of the detector. Correction factors are determined using both PYTHIA and CKKW MC samples. The Z + jets PYTHIA MC sample is generated using $f_i \bar{f}_i \to g Z^0$ and $f_i g \to f_i Z^0$ subprocesses, and it only contains particle level jets without detector simulation. An 8 GeV cutoff is applied at the jet reconstruction stage. The CKKW sample is described in Section 3.2.

In both PYTHIA and CKKW, the p_T values of the particle level jets are smeared with the data jet energy resolution. Subsequently, jets are removed from the sample, probabilistically, and according to the measured jet reconstruction efficiencies. The inclusive jet multiplicity spectra for both PYTHIA and CKKW are then compared to data in Figures 35 and 36. In the case of PYTHIA, there is increasing disagreement at higher jet multiplicities, since PYTHIA does not include higher order contributions at the hard scatter level. In the case of CKKW, the comparison is better, but still shows some disagreement. These discrepancies are corrected by taking the ratio between data and MC for each inclusive jet multiplicity and then applying these weights to the events. We also correct for differences in the jet p_T distributions (Figure 37 and 38), by applying additional corrective weights probabilistically. After these additional steps, the inclusive jet multiplicity as well as jet p_T and η distributions in PYTHIA and CKKW are again compared with data with much better agreement (Figures 39 to 56). These corrected PYTHIA and CKKW MC samples are used to derive the coefficients that unsmear the measured data jet multiplicities, also taking into account jet reco/ID inefficiencies.

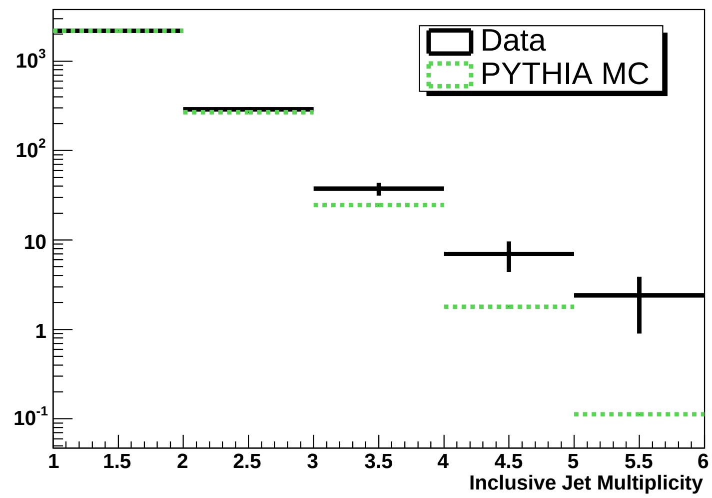

Figure 35: Comparison of inclusive jet multiplicities between data and particle level PYTHIA MC (applying data resolution smearing and data jet reco/ID efficiencies). The distributions are normalized with respect to the first bin. Only statistical uncertainties for data are shown.

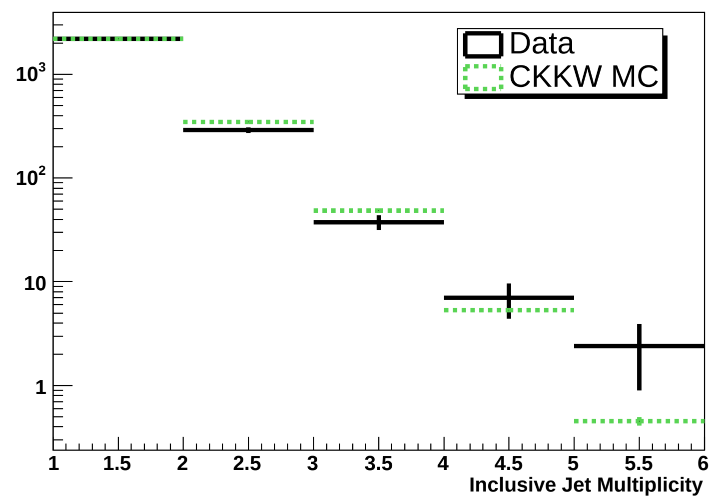

Figure 36: Comparison of inclusive jet multiplicities between data and particle level CKKW MC (applying data resolution smearing and data jet reco/ID efficiencies). The distributions are normalized with respect to the first bin. Only statistical uncertainties for data are shown.

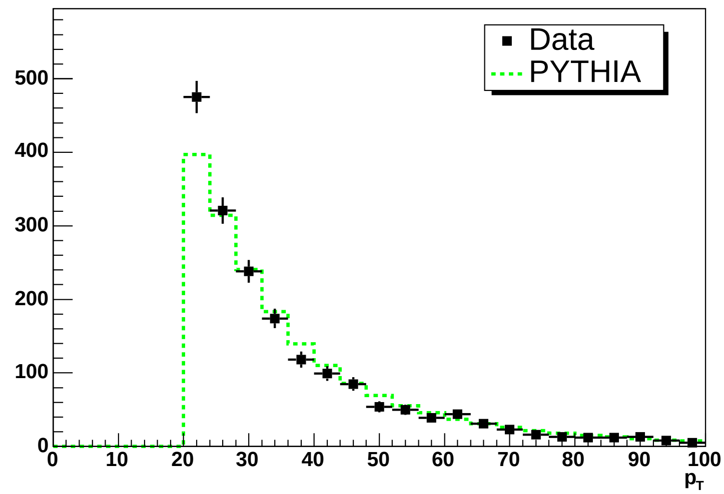

Figure 37: Comparison of jet p_T [GeV] for all jets between data and particle level PYTHIA MC (with data resolution smearing and jet reco/ID efficiencies applied). The MC distribution is normalized to the number of events in data.

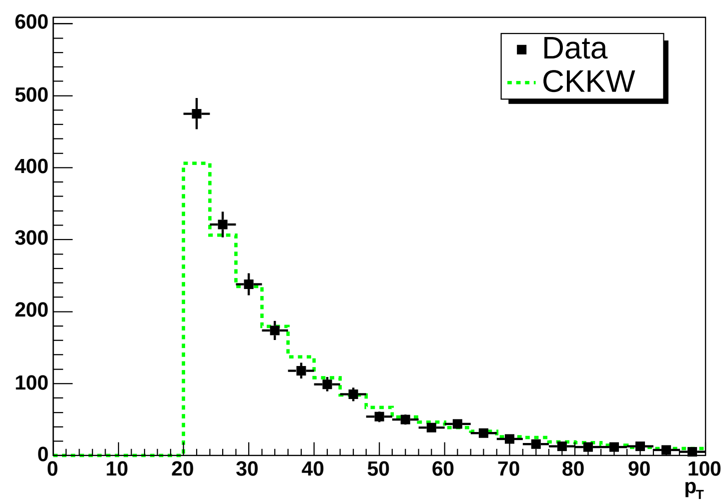

Figure 38: Comparison of jet p_T [GeV] for all jets between data and particle level CKKW MC (with data resolution smearing and jet reco/ID efficiencies applied). The MC distribution is normalized to the number of events in data.

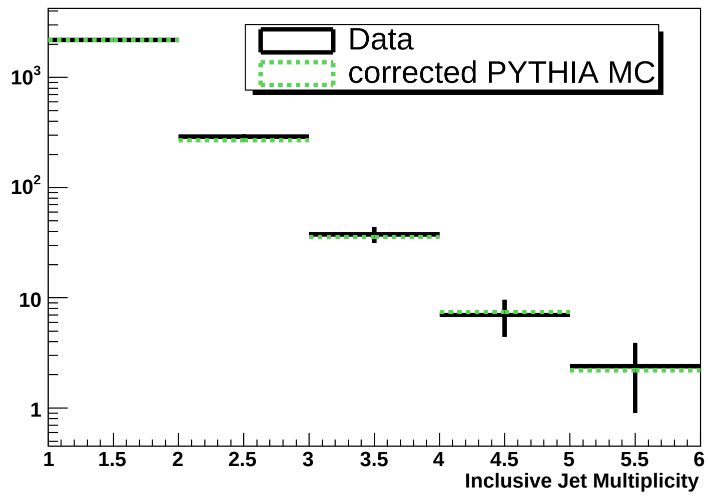

Figure 39: Comparison of corrected inclusive jet multiplicities between data and particle level PYTHIA MC (applying data resolution smearing and data jet reco/ID efficiencies). The distributions are normalized with respect to the first bin. Only statistical uncertainties for data are shown.

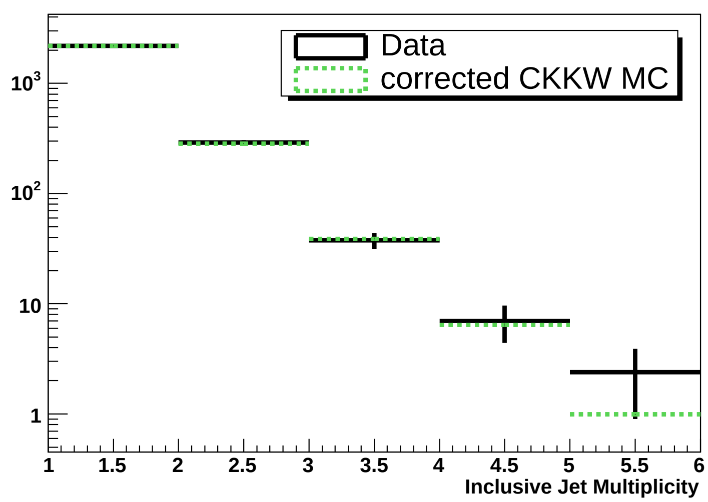

Figure 40: Comparison of corrected inclusive jet multiplicities between data and particle level CKKW MC (applying data resolution smearing and data jet reco/ID efficiencies). The distributions are normalized with respect to the first bin. Only statistical uncertainties for data are shown.

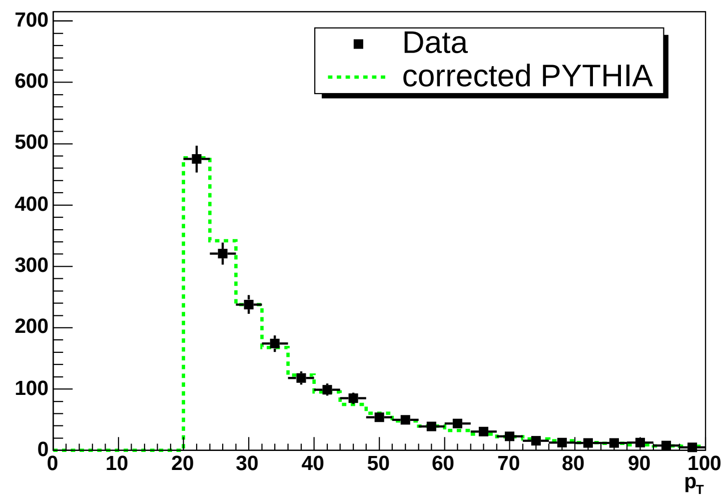

Figure 41: Comparison of corrected jet p_T [GeV] for all jets between data and particle level PYTHIA MC (with data resolution smearing and jet reco/ID efficiencies applied). The MC distribution is normalized to the number of events in data.

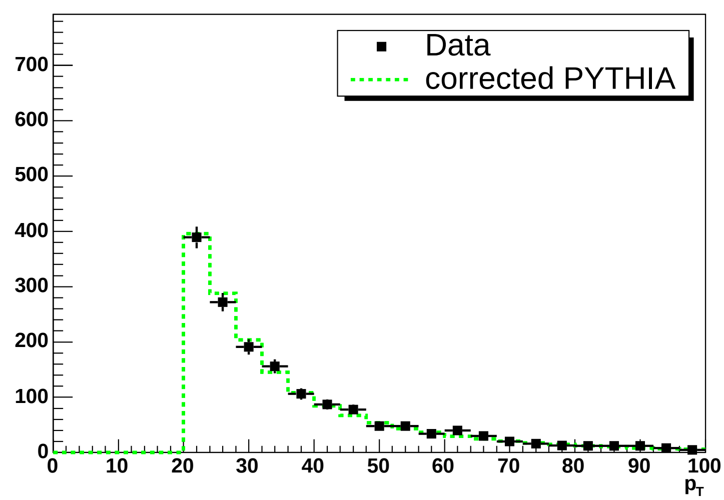

Figure 42: Comparison of corrected jet p_T [GeV] for leading jets between data and particle level PYTHIA MC (with data resolution smearing and jet reco/ID efficiencies applied). The MC distribution is normalized to the number of events in data.

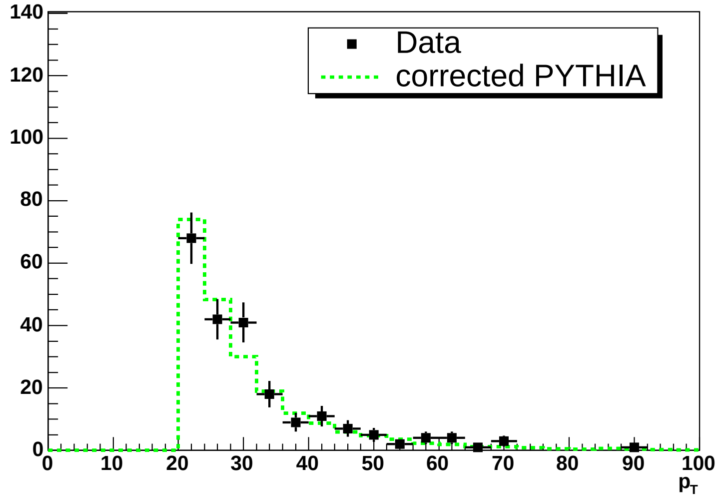

Figure 43: Comparison of corrected jet p_T [GeV] for second leading jets between data and particle level PYTHIA MC (with data resolution smearing and jet reco/ID efficiencies applied). The MC distribution is normalized to the number of events in data.

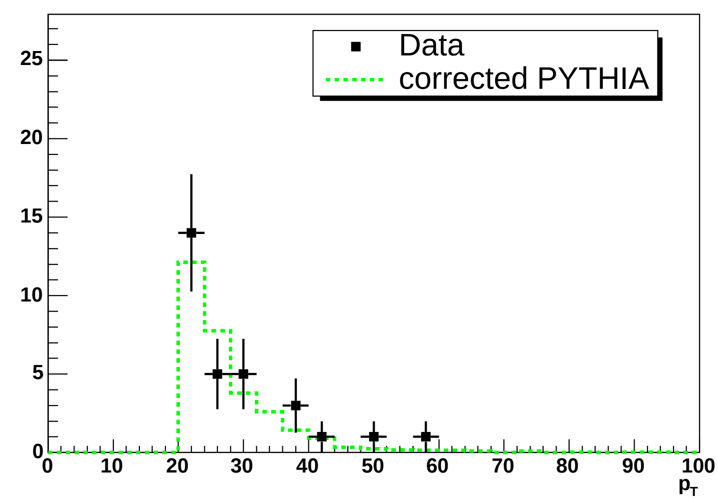

Figure 44: Comparison of corrected jet p_T [GeV] for third leading jets between data and particle level PYTHIA MC (with data resolution smearing and jet reco/ID efficiencies applied). The MC distribution is normalized to the number of events in data.

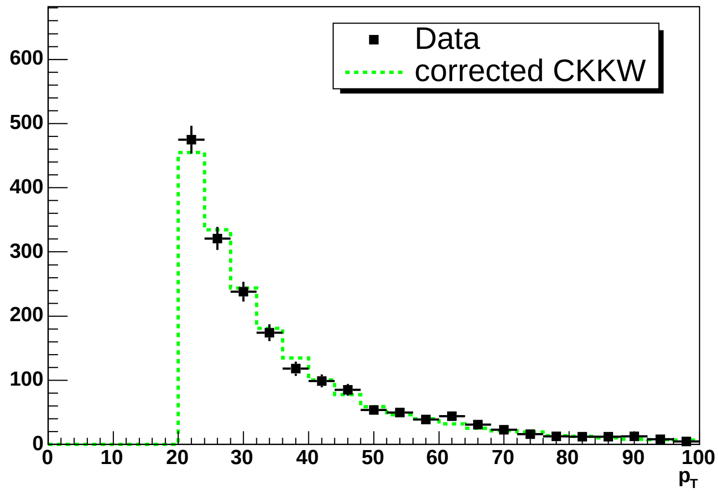

Figure 45: Comparison of corrected jet p_T [GeV] for all jets between data and particle level CKKW MC (with data resolution smearing and jet reco/ID efficiencies applied). The MC distribution is normalized to the number of events in data.

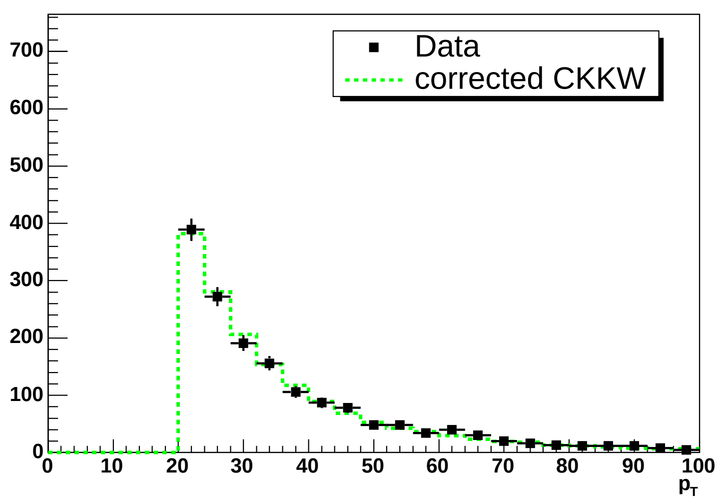

Figure 46: Comparison of corrected jet p_T [GeV] for leading jets between data and particle level CKKW MC (with data resolution smearing and jet reco/ID efficiencies applied). The MC distribution is normalized to the number of events in data.

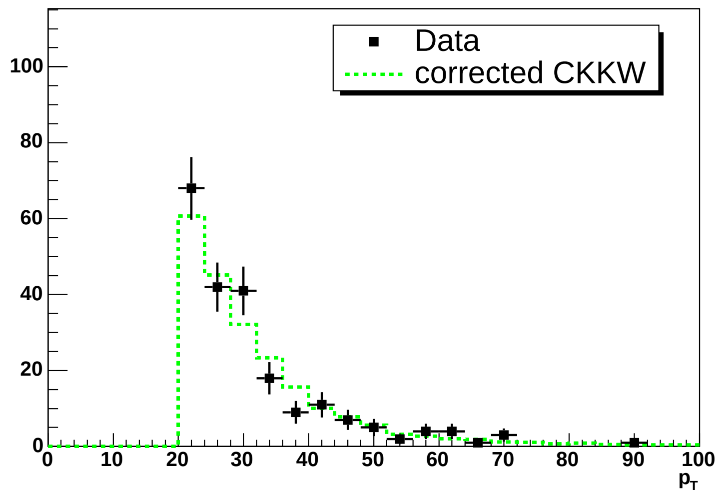

Figure 47: Comparison of corrected jet p_T [GeV] for second leading jets between data and particle level CKKW MC (with data resolution smearing and jet reco/ID efficiencies applied). The MC distribution is normalized to the number of events in data.

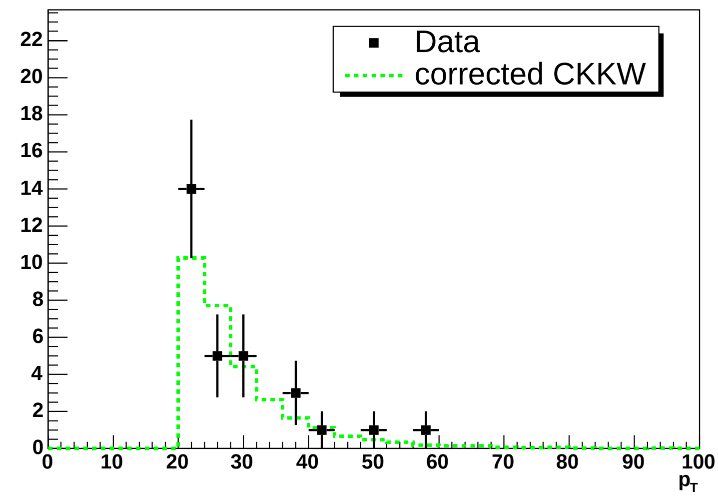

Figure 48: Comparison of corrected jet p_T [GeV] for third leading jets between data and particle level CKKW MC (with data resolution smearing and jet reco/ID efficiencies applied). The MC distribution is normalized to the number of events in data.

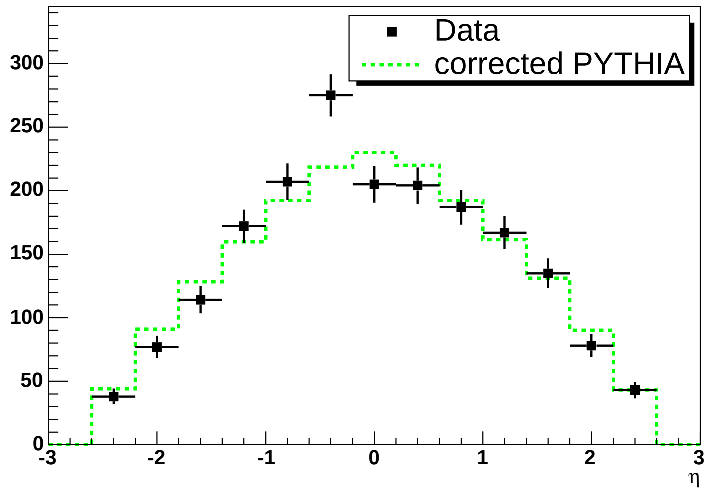

Figure 49: Comparison of corrected jet η for all jets between data and particle level PYTHIA MC (with data resolution smearing and jet reco/ID efficiencies applied). The MC distribution is normalized to the number of events in data.

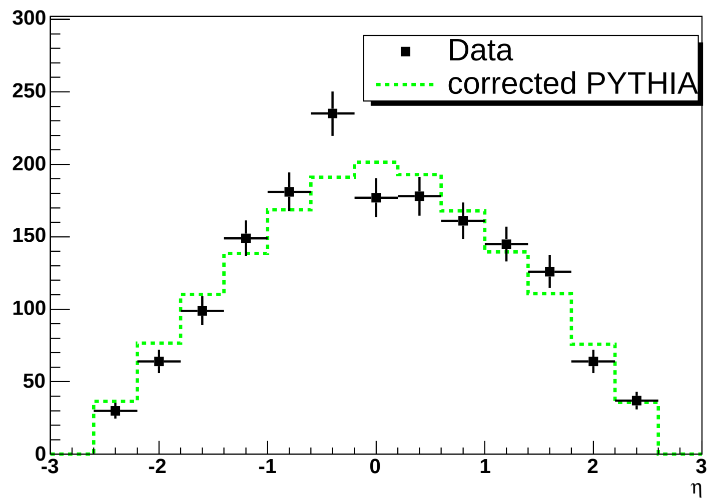

Figure 50: Comparison of corrected jet η for leading jets between data and particle level PYTHIA MC (with data resolution smearing and jet reco/ID efficiencies applied). The MC distribution is normalized to the number of events in data.

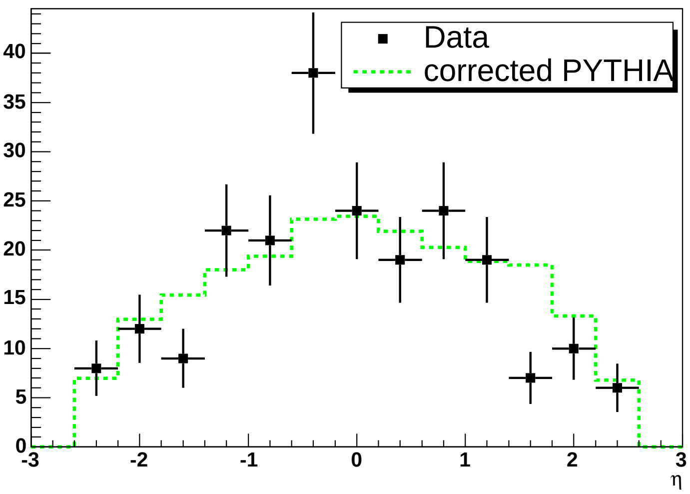

Figure 51: Comparison of corrected jet η for second leading jets between data and particle level PYTHIA MC (with data resolution smearing and jet reco/ID efficiencies applied). The MC distribution is normalized to the number of events in data.

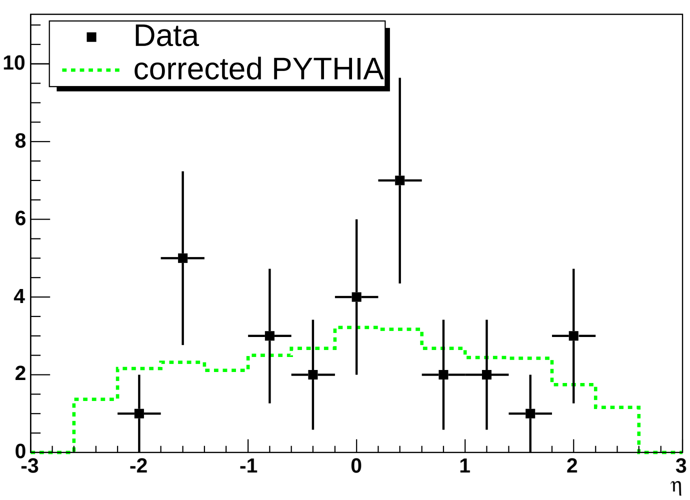

Figure 52: Comparison of corrected jet η for third leading jets between data and particle level PYTHIA MC (with data resolution smearing and jet reco/ID efficiencies applied). The MC distribution is normalized to the number of events in data.

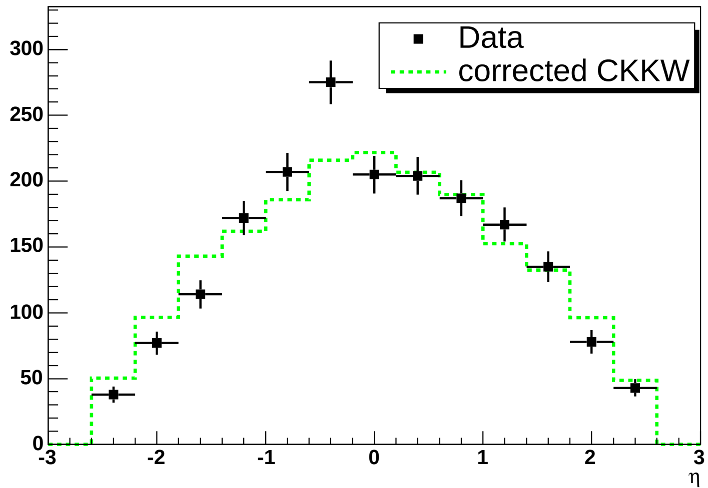

Figure 53: Comparison of corrected jet η for all jets between data and particle level CKKW MC (with data resolution smearing and jet reco/ID efficiencies applied). The MC distribution is normalized to the number of events in data.

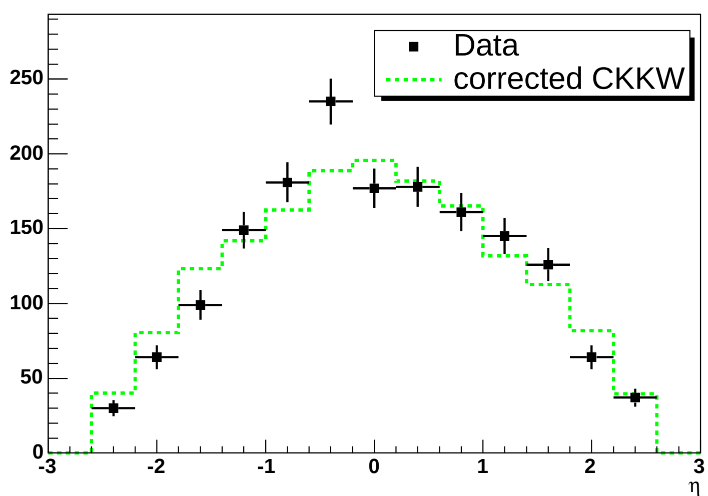

Figure 54: Comparison of corrected jet η for leading jets between data and particle level CKKW MC (with data resolution smearing and jet reco/ID efficiencies applied). The MC distribution is normalized to the number of events in data.

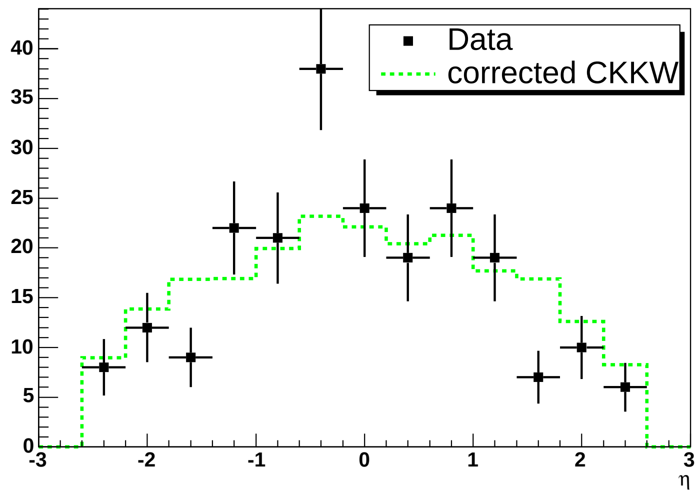

Figure 55: Comparison of corrected jet η for second leading jets between data and particle level CKKW MC (with data resolution smearing and jet reco/ID efficiencies applied). The MC distribution is normalized to the number of events in data.

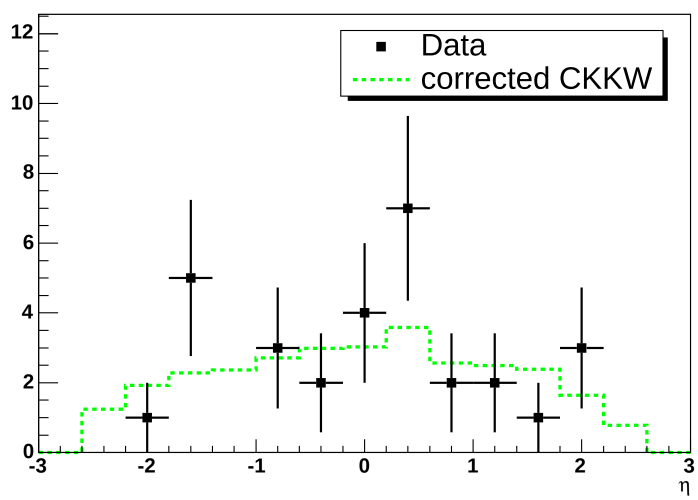

Figure 56: Comparison of corrected jet η for third leading jets between data and particle level CKKW MC (with data resolution smearing and jet reco/ID efficiencies applied). The MC distribution is normalized to the number of events in data.

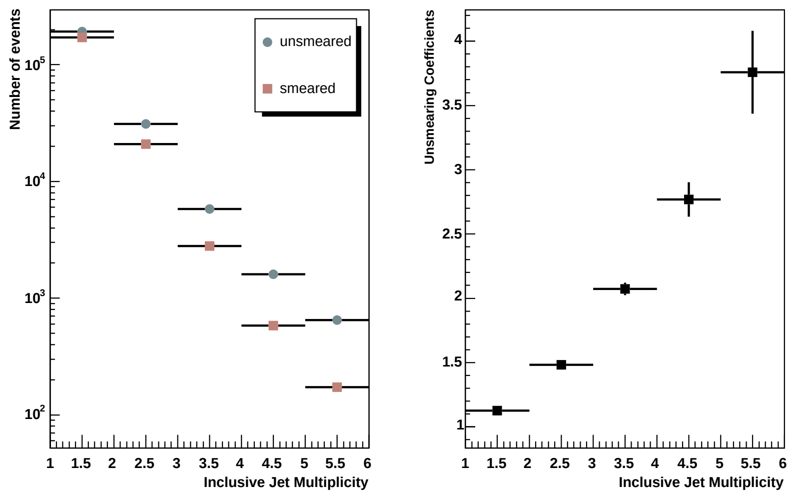

Figure 57: PYTHIA unsmearing and jet reco/ID particle jet multiplicities (left) and coefficients with statistical uncertainties (right).

To calculate the coefficients, the inclusive jet multiplicity histogram for particle level jets with $p_T > 20$ GeV and $|\eta_{physics}| < 2.5$ is divided by the inclusive jet multiplicity histogram for particle level jets with smeared $p_T > 20$ GeV and $|\eta_{physics}| < 2.5$ (after applying jet reco/ID efficiencies). In this fashion, we derive unsmearing and jet reco/ID coefficients based on both PYTHIA and CKKW MC. The final coefficients which are applied as multiplicative factors to the measured jet multiplicities in data are derived from the RMS weighted average between the PYTHIA and CKKW coefficients. Figures 57 and 58 show the numerator and denominator jet multiplicity histograms, as well as the ratio when applying jet smearing and jet reco/ID efficiencies in the denominator for PYTHIA and CKKW. Table 12 summarizes the PYTHIA and CKKW coefficients together with the final combined PYTHIA/CKKW coefficients. The statistical uncertainty of each unsmearing and jet reco/ID coefficient is used as a statistical uncertainty for the final cross sections (Section 8.10). The difference between the combined coefficients and the PYTHIA and CKKW coefficients is added as an additional systematic (Section 8.4).

In order to verify the unsmearing procedure outlined above, we derive unsmearing coefficients based on an alternative inverse matrix unfolding technique. Both methods yield similar unsmearing coefficients (within 2-3%). We also address the accuracy and possible limits of our unsmearing procedure by performing a closure test, and assigning an additional systematic uncertainty (Section 8.4).

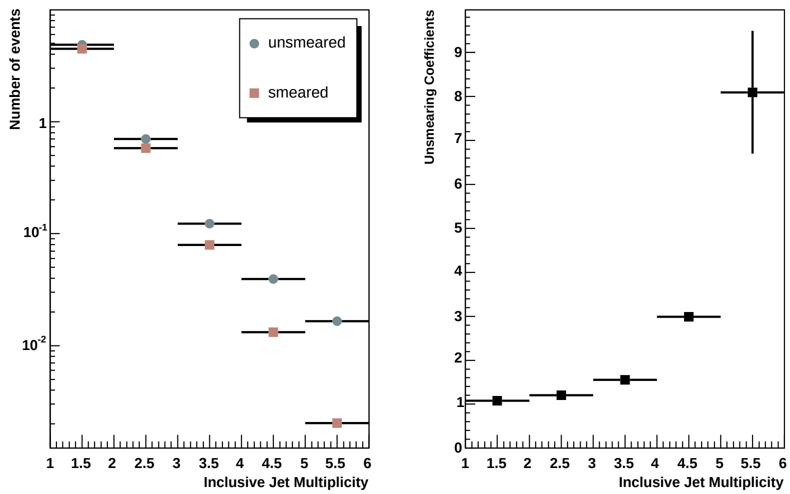

Figure 58: CKKW unsmearing and jet reco/ID particle jet multiplicities (left) and coefficients with statistical uncertainties (right).

Jet multiplicity	PYTHIA Coefficients	CKKW Coefficients	Combined Coefficients
≥ 1	1.125 $\pm$0.004	1.081 $\pm$0.006	1.111 $\pm$0.003
≥ 2	1.484 $\pm$0.015	1.204 $\pm$0.012	1.313 $\pm$0.009
≥ 3	2.073 $\pm$0.076	1.550 $\pm$0.026	1.605 $\pm$0.025
≥ 4	2.77 $\pm$0.18	2.99 $\pm$0.10	2.94 $\pm$0.09
≥ 5	3.76 $\pm$3.80	8.1 $\pm$1.4	7.58 $\pm$1.31

Table 12: PYTHIA, CKKW, and combined unsmearing and jet reco/ID coefficients with statistical uncertainties.

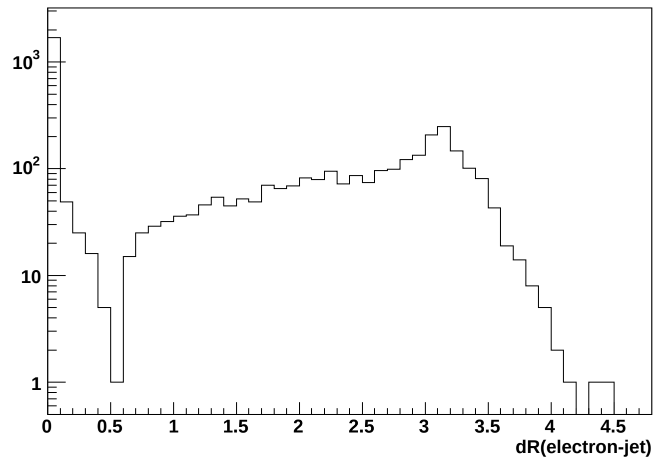

Figure 59: ΔR between probe tracks and good jets in data (without electron-jet-overlap cut).

7.2.2 Electron-Jet-Overlap Correction

The electron-jet-overlap correction provides an adjustment for the fraction of jets that are rejected due to an overlap with electrons from Z/γ^* decays.

Using the tag-and-probe method outlined in Section 6.1.2, the ΔR distribution between probe tracks and reconstructed jets that pass all jet quality cuts except for the electron-jet-overlap cut is plotted in data and MC (Figures 59 and 60).

There is an excess of entries at ΔR values of 0 and π due to fake jets (i.e. originated from the electron energy deposits) which survived the jet quality cuts. Therefore, all jets are rejected that are near either of the two electrons from Z/γ^* decays within ΔR=0.4. Figure 61 shows the same distribution as in Figure 59 after adding the electron-jet-overlap cut in data. For comparison Figure 62 shows the ΔR between generated Z/γ^* electrons and partons in MC.

A correction is derived in order to account for the real jets that are removed by the electron-jet-overlap cut. Using the same PYTHIA MC sample as for the unsmearing studies (see Section 7.2.1), the correction factors due to the electron-jet-overlap are estimated by taking the ratio of the inclusive parton multiplicity distribution for all partons with $p_T > 20$ GeV and $|\eta| <2.5$ and the inclusive parton multiplicity distribution for partons that are outside of the ΔR cone with respect to the electrons from the Z/γ^*.

Correction factors are derived per multiplicity bin using ΔR cones of size 0.4 and 0.7 and then taking the middle value as the final correction factors and the half difference as the systematic uncertainty. This is done in order to account for the position resolution between partons and calorimeter jets (see Figure 63).

Table 13 summarizes the electron-jet-overlap correction factors for different jet

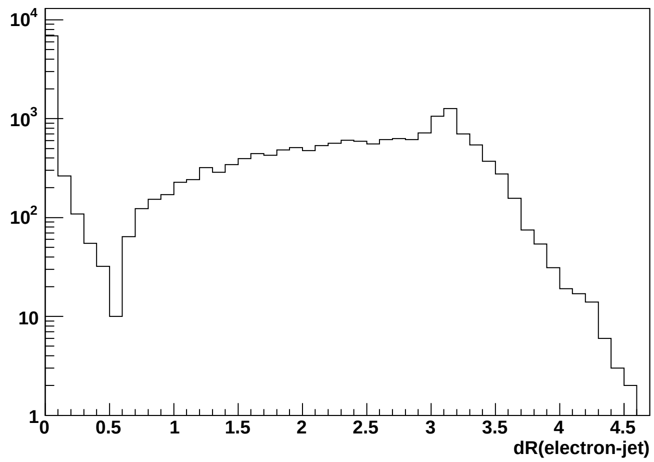

Figure 60: ΔR between probe tracks and good jets using PYTHIA MC (without electron-jet-overlap cut).

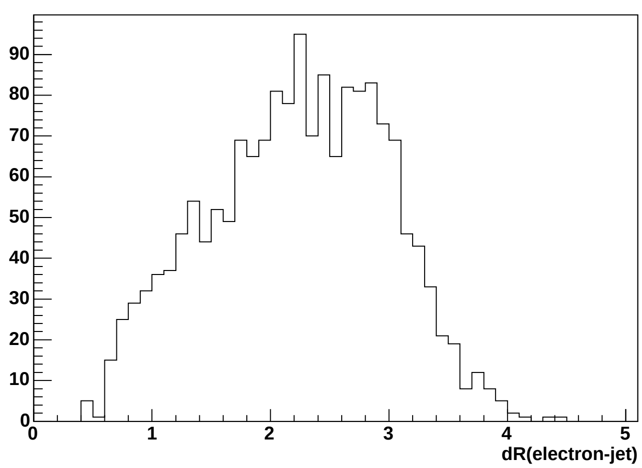

Figure 61: ΔR between probe tracks and good jets in data (after the electron-jet-overlap cut was applied).

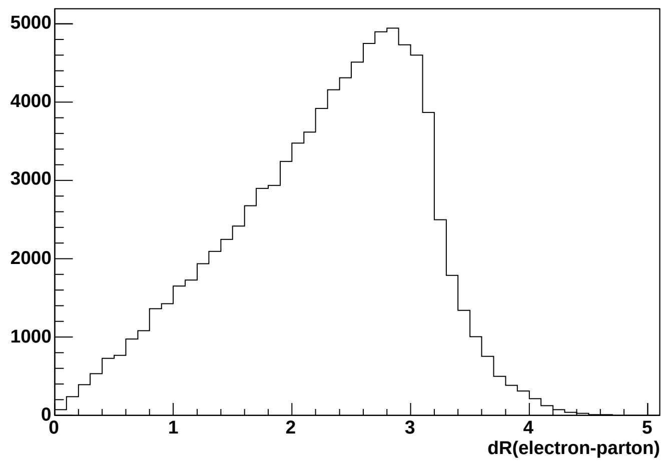

Figure 62: ΔR between generated electrons ($p_T > 25$ GeV, $|\eta| < 1.1$) and partons ($p_T > 20$ GeV, $|\eta| < 2.5$) in MC.

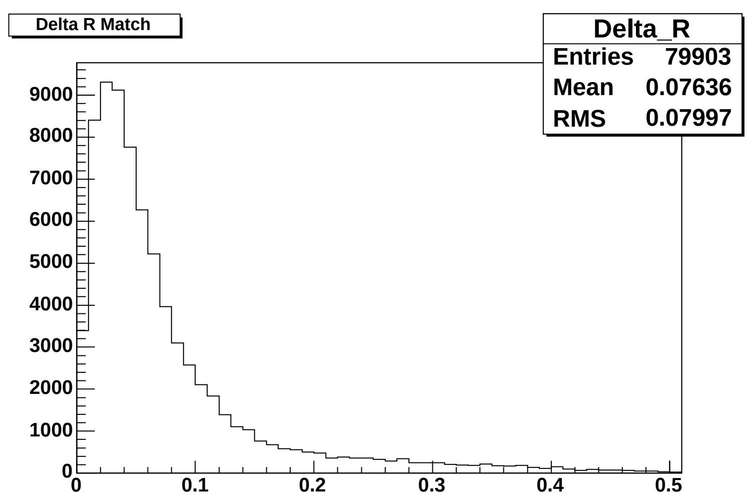

Figure 63: ΔR between partons and matched calorimeter jets ($p_T > 20$ GeV, $|\eta| < 2.5$) in MC.

Jet Multiplicity	Electron-Jet-Overlap Coefficient
≥ 1	1.059 $\pm$0.028
≥ 2	1.075 $\pm$0.041
≥ 3	1.092 $\pm$0.054
≥ 4	1.109 $\pm$0.067
≥ 5	1.125 $\pm$0.077

Table 13: Electron-Jet-Overlap coefficients with systematic uncertainties.

Jet Multiplicity	Signal	QCD	$W \rightarrow e\nu$	$Z \rightarrow \tau\tau$	$t\bar{t} \rightarrow l\nu bl\nu b$
≥ 1	2189.7	63.9	5.3	0.6	2.0
≥ 2	289.4	9.2	2.7	-	1.5
≥ 3	37.6	1.9	-	-	0.2
≥ 4	6.8	0.2	-	-	0.03
≥ 5	2.4	0.04	-	-	0.002

Table 14: Number of signal and background events at the detector level for different jet multiplicities.

multiplicity samples. These corrections are applied as multiplicative factors to the cross sections as a function of jet multiplicity in data.

7.2.3 Cross Sections

Figures 64 - 67 shows the diem invariant mass distributions for jet multiplicities $\geq$1 to $\geq$5 which are used to extract the number of signal and background events for the cross section calculation (corrected for trigger, EM and tracking inefficiencies). For jet multiplicities of $\geq$1 and $\geq$2, the same technique to extract the number of signal and background events is used as outlined in Section 6.2. For jet multiplicities of $\geq$3, sidebands are used to estimate the background. The background contributions for higher jet multiplicity samples were estimated by extrapolating an exponential fit to the QCD background of the 0 - 3 jet multiplicity bins (see Section 8.10).

Using the MC samples described in Section 3.4, we also estimate the small contributions from additional physics backgrounds.

Table 14 summarizes the number of signal and background events for each jet multiplicity. A 2.06% Drell-Yan contribution to the number of signal events is derived using the inclusive MC PYTHIA sample. The fully corrected and unsmeared cross sections versus jet multiplicities (with jet $p_T > 20$ GeV, $|\eta| < 2.5$) are shown in Figure 68 with statistical uncertainties.

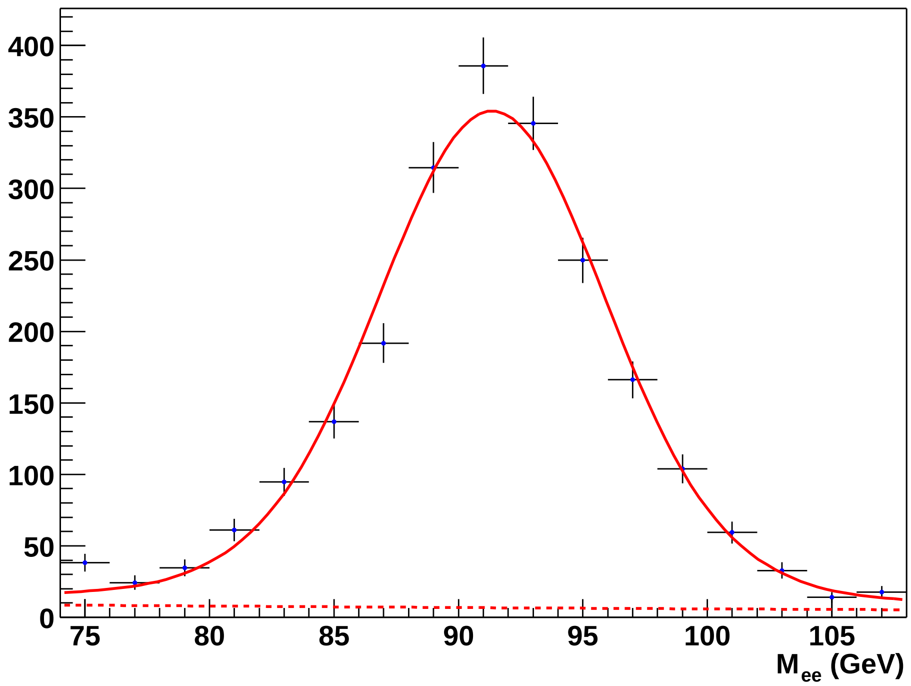

Figure 64: Diem invariant mass distribution for the $Z/\gamma^* \to e^+e^- + \geq 1$ jet sample. The solid line shows a Gaussian plus Breit-Wigner fit to the Z peak. The dashed line shows an exponential fit to the QCD and Drell-Yan contribution.

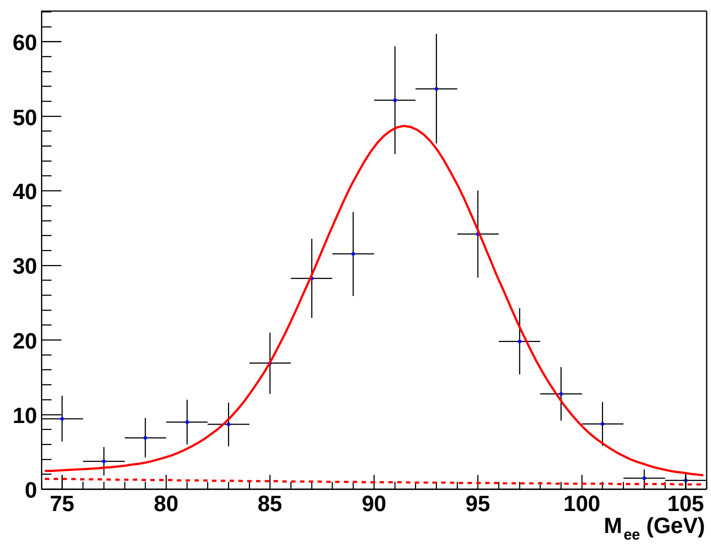

Figure 65: Diem invariant mass distribution for the $Z/\gamma^* \rightarrow e^+e^- + \geq 2$ jet sample. The solid line shows a Gaussian plus Breit-Wigner fit to the Z peak. The dashed line shows an exponential fit to the QCD and Drell-Yan contribution.

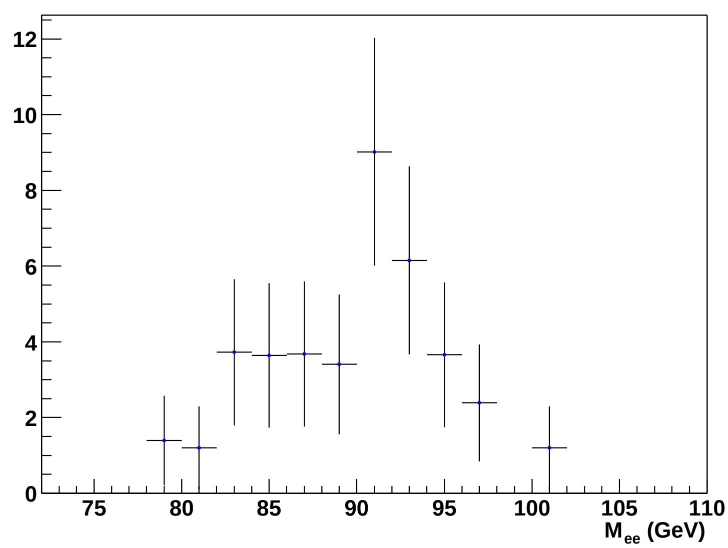

Figure 66: Diem invariant mass distribution for the $Z/\gamma^* \rightarrow e^+e^- + \geq 3$ jet sample.

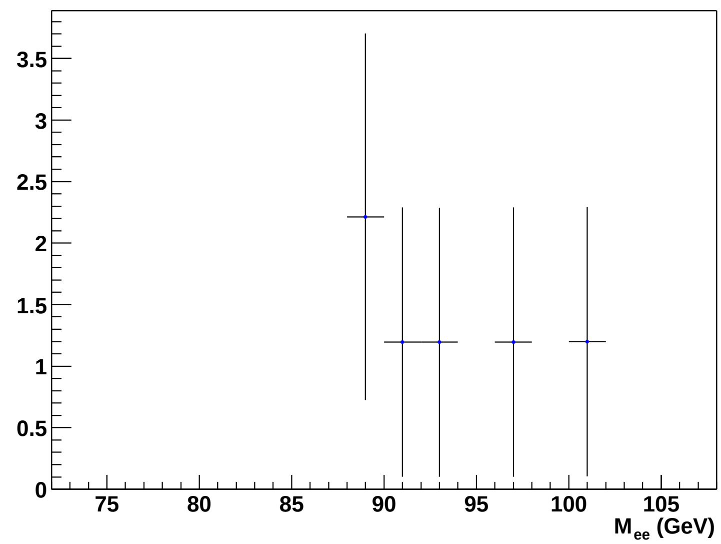

Figure 67: Diem invariant mass distribution for the $Z/\gamma^* \to e^+e^- + \geq 4$ jet sample.

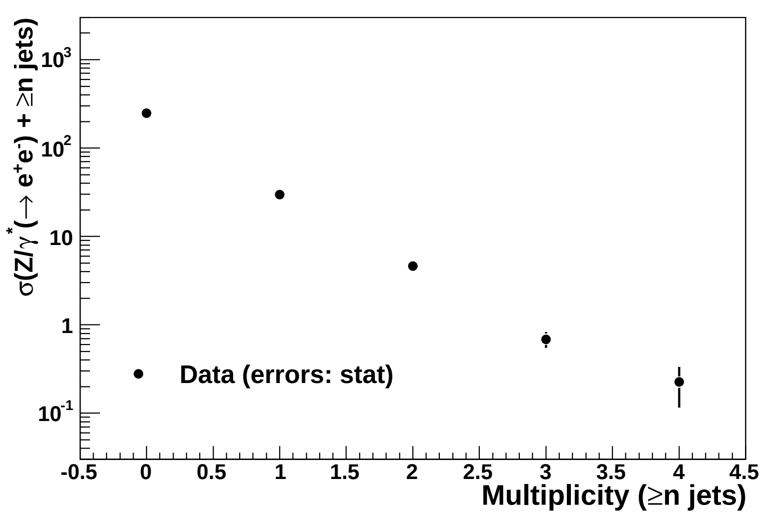

Figure 68: Fully corrected $Z/\gamma^*(\to e^+e^-)+ \geq n$ jet cross sections with statistical uncertainties.

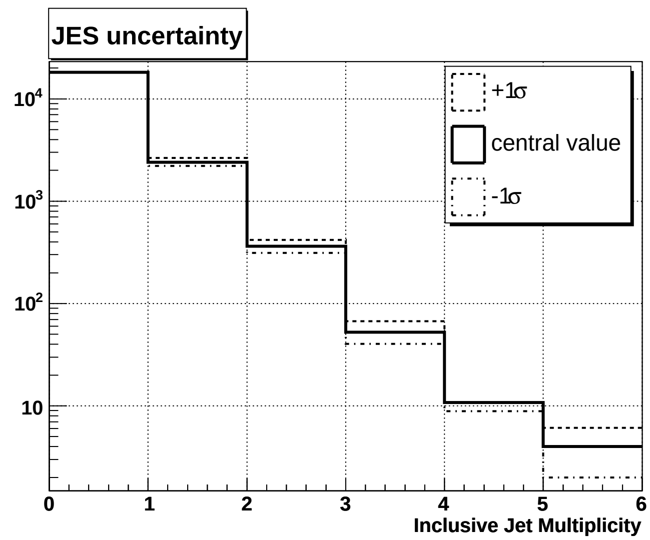

Figure 69: $\pm 1\sigma$ fluctuation of the jet energy scale (JES 5.3). The distributions are normalized with respect to the number of events in the 0-jet bin.

8 Systematic Uncertainties

In this section various sources for systematic uncertainties to the $Z + n$ jet cross section measurement are evaluated.

8.1 Jet Energy Scale Uncertainty

The uncertainty due to the jet energy scale (version 5.3) is estimated by varying the energy scale correction up and down by 1σ (combined systematic and statistical JES uncertainty in data) and subsequently recalculating the diem invariant mass histograms (corrected for trigger, EM reco/ID, and EM-Track matching inefficiencies) to get the number of corrected signal events for different jet multiplicities. After this step, the cross sections are recalculated to estimate the JES uncertainty. Figure 69 shows the effect of the JES uncertainty on the corrected jet multiplicity distribution. Table 15 summarizes the JES uncertainties.

Since the slope of the JES distributions in Figure 69 does not change much with respect to jet multiplicity, we assume uncorrelated JES uncertainties.

8.2 Jet Reco/ID Uncertainty

A detailed description of the jet reco/ID efficiency uncertainties can be found in Reference [20]. Figures 70, 71 and 72 show the jet reco/ID efficiencies with uncertainty bands for central, ICR, and forward rapidities. To estimate the

Jet multiplicity	Cross Section	JES Uncertainties
≥ 1	29.8 pb	± 2.9 pb
≥ 2	4.62 pb	± 0.83 pb
≥ 3	0.697 pb	± 0.185 pb
≥ 4	0.225 pb	± 0.057 pb

Table 15: Final cross sections with jet energy scale uncertainties.

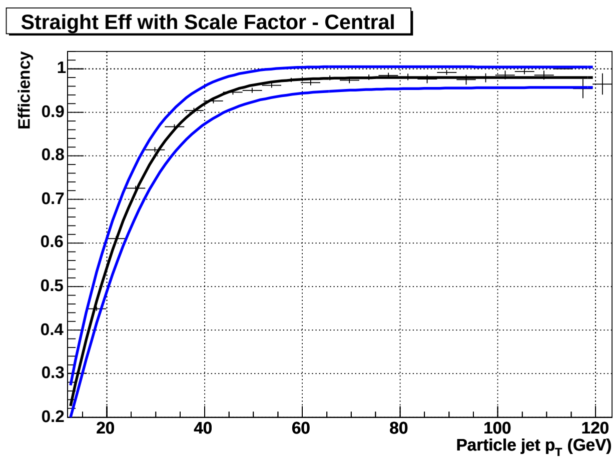

Figure 70: Jet reco/ID efficiencies with uncertainties plotted versus particle jet p_T smeared with data energy resolution (central).

jet reco/ID uncertainty, the unsmearing and jet reco/ID correction factors are rederived using the upper and lower uncertainty bands of the jet reco/ID efficiencies. Table 16 summarizes the jet reco/ID uncertainties.

8.3 Jet Energy Resolution Uncertainty

The parameterization of the jet energy resolution used in this analysis is based on JES 5.0 with T42 applied (see Section 3.1). The difference between JES 5.0 and a later parameterization (JES 5.3) is taken into account as an additional systematic uncertainty. The estimation of the systematic uncertainty is based on a comparison between JES 5.1 (equivalent to JES 5.0) and JES 5.3 parameterizations (Figure 73). The comparison shows a difference of approximately 5% between JES 5.1 and 5.3 [21]. A conservative uncertainty of 10% is assigned to account for this difference. Subsequently, the uncertainty due to jet energy resolution smearing in the unsmearing procedure is derived by varying the data jet energy resolution by $\pm$ 10%. Table 17 summarizes the jet resolution uncertainties.

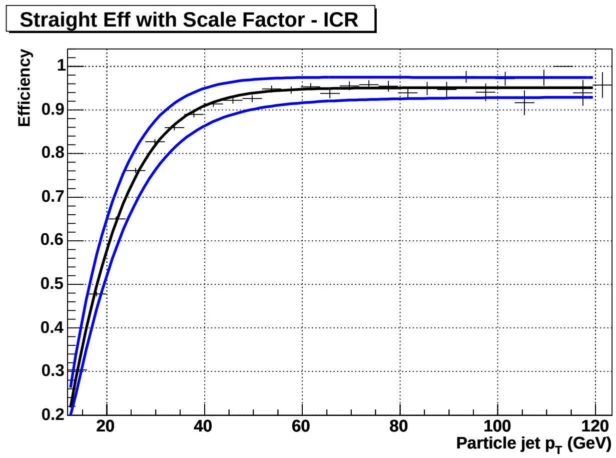

Figure 71: Jet reco/ID efficiencies with uncertainties plotted versus particle jet p_T smeared with data energy resolution (ICR).

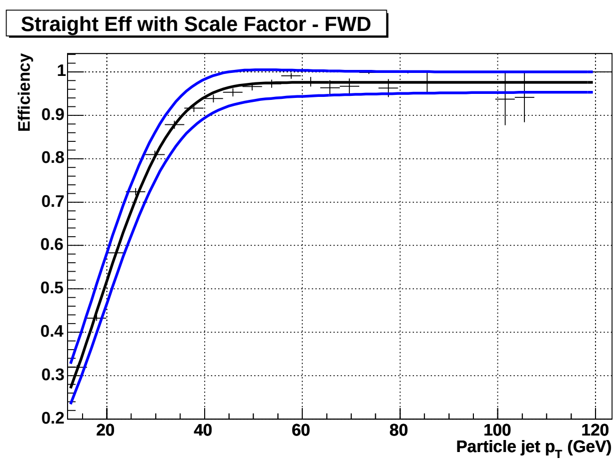

Figure 72: Jet reco/ID efficiencies with uncertainties plotted versus particle jet p_T smeared with data energy resolution (forward).

Jet multiplicity	Cross Section	Jet Reco/ID Uncertainties
≥ 1	29.8 pb	$^{+0.5}_{-1.7}$pb
≥ 2	4.62 pb	$^{+1.06}_{-0.71}$pb
≥ 3	0.697 pb	$^{+0.202}_{-0.160}$pb
≥ 4	0.225 pb	$^{+0.099}_{-0.075}$pb

Table 16: Final cross sections with jet reco/ID uncertainties.

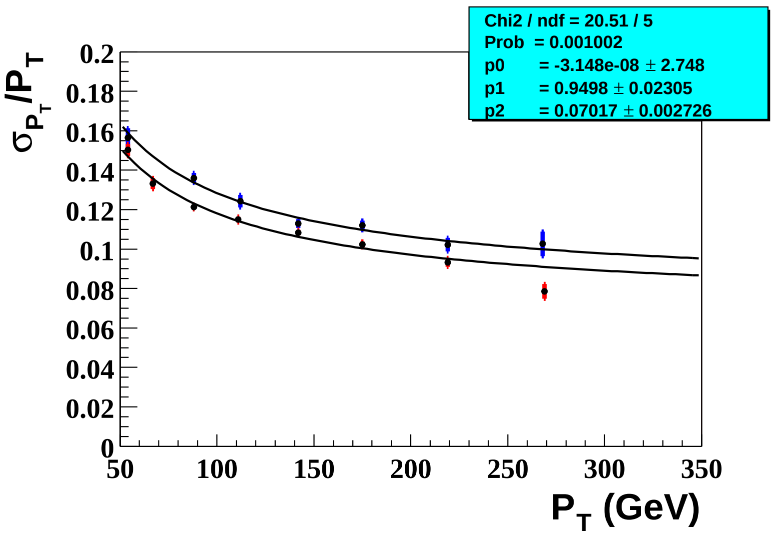

Figure 73: Comparison of jet energy resolution for JES 5.1 (upper curve) and JES 5.3 (lower curve) in the central region of the Calorimeter. The difference is approximately 5% over the whole range.

Jet Multiplicity	Cross Section	Jet Energy Resolution Uncertainties
≥ 1	29.8 pb	$\pm$0.8 pb
≥ 2	4.62 pb	$\pm$0.03 pb
≥ 3	0.697 pb	$\pm$0.042 pb
≥ 4	0.225 pb	$\pm$0.009 pb

Table 17: Final cross sections with jet energy resolution uncertainties.

8.4 Unsmearing Uncertainty

We verify the accuracy of the unsmearing procedure by performing a closure test. In this test we apply data resolution smearing and jet reco/ID efficiencies to the PYTHIA unsmearing sample and assume that it is data. We then use the CKKW sample to unsmear it. Table 18 compares the expected and derived unsmearing and jet reco/ID coefficients. The difference between the two is added as an additional unsmearing systematic (Table 19).

Since the final unsmearing and jet reco/ID coefficients are averages derived from PYTHIA and CKKW coefficients, we add an additional systematic uncertainty based on the difference between the combined and the PYTHIA and CKKW values (Table 20).

Jet Multiplicity	Expected Coefficient	Derived Coefficient
≥ 1	1.056 ± 0.003	1.070 ± 0.005
≥ 2	1.133 ± 0.011	1.134 ± 0.006
≥ 3	1.213 ± 0.039	1.118 ± 0.018
≥ 4	1.336 ± 0.162	1.220 ± 0.053

Table 18: Expected and derived unsmearing and jet reco/ID coefficients with statistical uncertainties.

Jet Multiplicity	Cross Section	Unsmearing Uncertainties
≥ 1	29.8 pb	± 0.4 pb
≥ 2	4.62 pb	± 0.01 pb
≥ 3	0.697 pb	± 0.054 pb
≥ 4	0.225 pb	± 0.020 pb

Table 19: Final cross sections with unsmearing uncertainties from closure test.

Jet Multiplicity	Cross Section	Unsmearing Uncertainties
≥ 1	29.8 pb	+0.4 pb -0.8 pb
≥ 2	4.62 pb	+0.60 pb -0.38pb
≥ 3	0.697 pb	+0.203 pb -0.024 pb
≥ 4	0.225 pb	+0.013 pb -0.004pb

Table 20: Final cross sections with unsmearing uncertainties due to the difference between combined and PYTHIA/CKKW unsmearing and jet reco/ID coefficients.

Jet Multiplicity	ALPGEN Acceptance	CKKW Acceptance
≥ 1	$(25.1 \pm 0.2)\%$	$(24.4 \pm 0.2)\%$
≥ 2	$(25.4 \pm 0.2)\%$	$(25.2 \pm 0.2)\%$
≥ 3	$(27.4 \pm 0.3)\%$	$(25.2 \pm 0.2)\%$
≥ 4	$(28.5 \pm 0.7)\%$	$(27.2 \pm 0.3)\%$

Table 21: Comparing acceptances with statistical uncertainties between ALPGEN (CTEQ5L) and CKKW (CTEQ6L) for different jet multiplicities.

Jet Multiplicity	Cross Section Ratio $[\cdot 10^{-3}]$	Acceptance Uncertainties $[\cdot 10^{-3}]$
≥ 1	120.1	± 1.8
≥ 2	18.6	± 0.7
≥ 3	2.8	± 0.1
≥ 4	0.90	± 0.003

Table 22: Final cross section ratios with acceptance uncertainties.

8.5 Acceptance Uncertainty

Using CKKW MC samples, we derive acceptances for different jet multiplicities following the procedure outlined in Section 7.1.4. Table 21 compares the CKKW acceptances with the previously derived ALPGEN MC acceptances. Since our final goal is to measure cross sections normalized with respect to the inclusive $Z/\gamma^* \to e^+e^-$ cross section, we calculate the $(Z + n\,\text{jet}/Z\ \text{inclusive})$ acceptance ratios for both ALPGEN and CKKW, and take the difference for each jet multiplicity as a systematic uncertainty. This uncertainty takes into account varying PDFs and Q^2 values. Table 22 summarizes the acceptance uncertainties.

8.6 Systematic Uncertainty Due to Efficiencies

In the following, the systematic uncertainties of the object based efficiencies are taken from Sections 7.1.1 to 7.1.3, converted into event based systematic uncertainties, and then propagated to the cross sections.

8.6.1 Trigger Efficiency

A relative systematic uncertainty to the cross section of $\pm 1\%$ is estimated due to the variations in the trigger efficiencies versus jet multiplicity (see Section 7.1.1). The uncertainties are estimated based on the following equations:

$$\varepsilon_{Object}(\text{pre-v12, inclusive sample}) = 94.6\%, \quad \delta\varepsilon_{Object} = 5\% \tag{16}$$

$$\varepsilon_{Event} = 2 \cdot \varepsilon_{Object} - \varepsilon^2_{Object} = 99.7\% \tag{17}$$

$$\delta\varepsilon_{Event}(-1\sigma) = 2 \cdot (\varepsilon_{Object} - \delta\varepsilon_{Object}) - (\varepsilon_{Object} - \delta\varepsilon_{Object})^2 = 98.9\% \tag{18}$$

$$\text{Relative Uncertainty} = \frac{99.7\% - 98.9\%}{99.7\%} = 0.8\% \approx 1\%. \tag{19}$$

Jet Multiplicity	Relative Uncertainty
≥ 1	0.5%
≥ 2	1.5%
≥ 3	2.3%
≥ 4	3.7%
≥ 5	5.5%

Table 23: Relative uncertainties due to uncertainty in EM-Track matching efficiencies.

8.6.2 EM Reconstruction and Identification Efficiency

A relative systematic uncertainty to the cross section of $\pm 7\%$ is assumed due to the variations in the EM reco and ID efficiencies versus jet multiplicity (see Section 7.1.2). The uncertainties are estimated based on the following equations:

$$\varepsilon_{Object}(\text{data, inclusive sample}) = 88.9\%, \quad \delta\varepsilon_{Object} = 3\% \tag{20}$$

$$\varepsilon_{Event} = \varepsilon^2_{Object} = 79.0\% \tag{21}$$

$$\delta\varepsilon_{Event}(-1\sigma) = (\varepsilon_{Object} - \delta\varepsilon_{Object})^2 = 73.8\% \tag{22}$$

$$\text{Relative Uncertainty} = \frac{79.0\% - 73.8\%}{79.0\%} = 6.6\% \approx 7\%. \tag{23}$$

8.6.3 EM-Track Match Efficiency

Table 23 summarizes the relative systematic uncertainties to the cross section due to the variations in the EM-Track matching efficiencies versus jet multiplicity (see Section 7.1.3). The uncertainties are estimated based on the following equations:

$$\varepsilon_{Object}(\text{data, n-jet sample}) = \varepsilon_n, \quad \delta\varepsilon_{Object}(\text{data, n-jet sample}) = \delta\varepsilon_n \tag{24}$$

$$\varepsilon_{Event} = 2 \cdot \varepsilon_n - \varepsilon_n^2 \tag{25}$$

$$\delta\varepsilon_{Event}(-1\sigma) = 2 \cdot (\varepsilon_n - \delta\varepsilon_n) - (\varepsilon_n - \delta\varepsilon_n)^2 \tag{26}$$

$$\text{Relative Uncertainty} = \frac{\varepsilon_{Event} - \varepsilon_{Event}(-1\sigma)}{\varepsilon_{Event}}. \tag{27}$$

8.6.4 Overall Efficiency Systematic Uncertainty

Table 24 summarizes the overall systematic uncertainties of the cross sections versus jet multiplicity due to the efficiencies after adding all contributions in quadrature.

Jet Multiplicity	Cross Section	Efficiency Uncertainties
≥ 1	29.8 pb	$\pm$2.1 pb
≥ 2	4.62 pb	$\pm$0.33 pb
≥ 3	0.697 pb	$\pm$0.051 pb
≥ 4	0.225 pb	$\pm$0.017 pb

Table 24: Overall systematic uncertainties due to efficiencies (Trigger, EM, Tracking).

Jet Multiplicity	Cross Section	Electron-jet-overlap Uncertainties
≥ 1	29.8 pb	$\pm$0.8 pb
≥ 2	4.62 pb	$\pm$0.18 pb
≥ 3	0.697 pb	$\pm$0.035 pb
≥ 4	0.225 pb	$\pm$0.014 pb

Table 25: Final cross sections with electron-jet-overlap cut uncertainties.

8.7 Electron-Jet-Overlap Systematic Uncertainty

For each jet multiplicity, electron-jet-overlap correction factors are derived using ΔR=0.4 and ΔR=0.7 rejection cones and taking the middle value as the final correction. The systematic uncertainty is estimated by the difference between the middle values and the correction factors derived with ΔR=0.4 and ΔR=0.7.

Table 25 summarizes the systematic uncertainties for the electron-jet-overlap cut.

8.8 Luminosity Systematic Uncertainty

The uncertainty due to the uncertainty in the luminosity measurement is 6.5% [22]. Table 26 summarizes the luminosity uncertainties.

8.9 Jet Promotion Systematic Uncertainty

The measurement of the $Z/\gamma^* \rightarrow e^+e^- + \geq n$ jet cross section depends on a precise determination of jet multiplicities for each event. Therefore, the effect of additional jets from multiple interactions within the same beam crossing

Jet multiplicity	Cross Section	Luminosity Uncertainties
≥ 0	248.4 pb	$\pm$16.1 pb
≥ 1	29.8 pb	$\pm$1.9 pb
≥ 2	4.62 pb	$\pm$0.30 pb
≥ 3	0.697 pb	$\pm$0.045 pb
≥ 4	0.225 pb	$\pm$0.015 pb

Table 26: Final cross sections with luminosity uncertainties.

Jet multiplicity	Exactly one primary vertex	At least two primary vertices
≥ 0	5,900	5,900
≥ 1	705	696
≥ 2	92	97
≥ 3	11	16
≥ 4	3	1
≥ 5	1	1

Table 27: Number of events for different inclusive jet multiplicities when requiring exactly one reconstructed primary vertex and at least two reconstructed primary vertices. Entries are normalized with respect to the 2 vertex sample.

Jet multiplicity	Average number of primary vertices
≥ 1	1.583 ± 0.852
≥ 2	1.622 ± 0.911
≥ 3	1.733 ± 0.814
≥ 4	1.4 ± 0.8
≥ 5	2.0 ± 1.0

Table 28: Average number of reconstructed primary vertices for different jet multiplicities.

(*jet promotion*) is studied. Jet multiplicities of events that have exactly one reconstructed primary vertex are compared with events that have at least two reconstructed primary vertices (Table 27).

The two samples are normalized with respect to the number of events in the inclusive jet multiplicity bin. Initially the single vertex sample contains 7,848 events and the 2 (or more) vertex sample contains 5,900 events.

The jet promotion effect is small since the discrepancy between the two samples is within the statistical uncertainty.

Table 28 shows the average number of reconstructed primary vertices for different jet multiplicity samples. Since this number does not change statistically versus jet multiplicity, a bias due to additional $p\bar{p}$ interactions should be negligible.

8.10 Statistical Uncertainty

The statistical uncertainty of the cross sections includes the following components:

- The uncertainty due to the total number of corrected events $\delta \mathrm{N}_{corr}$ (corrected for Trigger, EM and Tracking inefficiencies) is estimated based on the following equations:

$$\mathrm{N}_{corr} = \mathrm{w}_{average} \cdot \mathrm{N}_{uncorr} \tag{28}$$

$$\Rightarrow \quad \delta \mathrm{N}_{corr} = \sqrt{(\mathrm{w}_{average} \cdot \delta \mathrm{N}_{uncorr})^2 + (\mathrm{N}_{uncorr} \cdot \delta \mathrm{w}_{average})^2}, \tag{29}$$

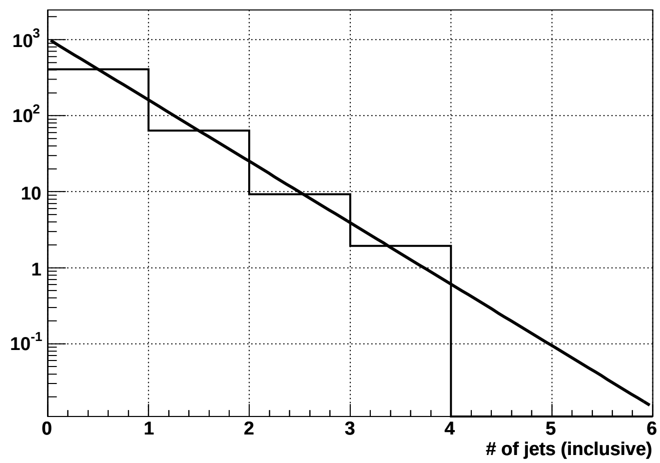

Figure 74: Exponential fit to the number of background events for different inclusive jet multiplicities.

where N_{corr} is the total number of corrected events, N_{uncorr} is the total number of uncorrected events, and $w_{average}$ is the average weight used to correct for EM, Trigger and Tracking inefficiencies (≈1.36).

- The uncertainty due to the number of background events δB is estimated by fitting an exponential function $a \cdot \exp(\ b \cdot \mathrm{x}\ )$ to the measured number of QCD events (Figure 74), and then propagating the uncertainty of the two fitting parameters a and b. The uncertainty of the exponential fit takes into account that the fitting parameters a and b are correlated:

$$f(x) = a \cdot exp(b \cdot x) \tag{30}$$

$$\delta f(x) = \sqrt{\left(\frac{\partial f}{\partial a} \cdot \delta a\right)^2 + \left(\frac{\partial f}{\partial b} \cdot \delta b\right)^2 + 2 \cdot \frac{\partial f}{\partial a} \cdot \frac{\partial f}{\partial b} \cdot covariance(a,b)}. \tag{31}$$

- The statistical uncertainty of the acceptances (see Table 11).

- The statistical uncertainty due to the unsmearing and jet reco/ID coefficients (see Section 7.2.1). This component is only relevant for jet multiplicities ≥ 1.

Table 29 summarizes the statistical uncertainties.

Jet Multiplicity	Cross Section	Total Statistical Uncertainty
≥ 0	248.4 pb	$\pm$2.5 pb
≥ 1	29.8 pb	$\pm$0.8 pb
≥ 2	4.62 pb	$\pm$0.34 pb
≥ 3	0.697 pb	$\pm$0.140 pb
≥ 4	0.225 pb	$\pm$0.109 pb

Table 29: Cross sections with total statistical uncertainties to the cross sections.

	$\geq$1 jet	$\geq$2 jets	$\geq$3 jets	$\geq$4 jets
$\frac{\sigma(Z/\gamma^*(\to e^+e^-)+\geq nJets)}{\sigma_{Z/\gamma^*}}$ $[\cdot 10^{-3}]$	120.1	18.6	2.8	0.90
Jet Energy Scale	$\pm$11.7	$\pm$3.3	$\pm$0.74	$\pm$0.23
Jet Reco/ID	$^{+2.2}_{-7.0}$	$^{+4.3}_{-2.9}$	$^{+0.82}_{-0.64}$	$^{+0.40}_{-0.30}$
Jet Energy Resolution	$^{+3.4}_{-2.7}$	$^{+0.13}_{-0.04}$	$^{+0.15}_{-0.17}$	$^{+0.04}_{-0.03}$
Unsmearing (Closure Test)	$\pm$1.6	$\pm$0.02	$\pm$0.22	$\pm$0.08
Unsmearing (MC Generators)	$^{+1.5}_{-3.2}$	$^{+2.4}_{-1.6}$	$^{+0.82}_{-0.10}$	$^{+0.05}_{-0.02}$
Acceptance	$\pm$1.8	$\pm$0.7	$\pm$0.10	$\pm$0.003
Efficiencies (Trigger, EM, Track)	$\pm$8.5	$\pm$1.3	$\pm$0.20	$\pm$0.07
Electron-Jet-Overlap	$\pm$3.2	$\pm$0.7	$\pm$0.14	$\pm$0.05

Table 30: Summary of systematic uncertainties for the cross section ratios.

	$\geq$1 jet	$\geq$2 jets	$\geq$3 jets	$\geq$4 jets
$\frac{\sigma(Z/\gamma^*(\to e^+e^-)+\geq nJets)}{\sigma_{Z/\gamma^*}}$ $[\cdot 10^{-3}]$	120.1	18.6	2.8	0.90
Number of Signal Events	$\pm$3.2	$\pm$1.3	$\pm$0.55	$\pm$0.44
Acceptance	$\pm$1.0	$\pm$0.1	$\pm$0.03	$\pm$0.02
Unsmearing	$\pm$0.3	$\pm$0.1	$\pm$0.04	$\pm$0.03

Table 31: Summary of statistical uncertainties for the cross section ratios.

8.11 Summary of Uncertainties

Tables 30 and 31 summarize systematic and statistical uncertainties for the cross section ratios.

9 Conclusions

The $Z/\gamma^*(\to e^+e^-)+\geq n$ jet cross sections for jet multiplicities of 0 to 4 have been measured for jets with $p_T > 20$ GeV and $|\eta| < 2.5$. The results are presented in terms of cross section ratios normalized with respect to the inclusive cross section. For cross section ratios, R_n, the luminosity measurement uncertainties cancel. All other systematic uncertainties contribute as shown in

Jet Multiplicity	# of Signal Events	$Z/\gamma^*(\rightarrow e^+e^-)+\geq n$ Jet Cross Section
≥ 0	18,223.5	248.4 pb $\pm$2.5(stat) $\pm$10.4(sys) $\pm$16.1(lumi)
≥ 1	2,566.8	29.8 pb $\pm$0.82(stat) $^{+3.8}_{-4.2}$(sys) $\pm$1.9(lumi)
≥ 2	402.6	4.62 pb $\pm$0.34(stat) $^{+1.5}_{-1.2}$(sys) $\pm$0.30(lumi)
≥ 3	65.5	0.697 pb $\pm$0.14(stat) $^{+0.35}_{-0.26}$(sys) $\pm$0.045(lumi)
≥ 4	21.95	0.225 pb $\pm$0.109(stat) $^{+0.119}_{-0.099}$(sys) $\pm$0.015(lumi)

Table 32: Number of fully corrected and unsmeared signal events and cross sections with statistical, systematic, and luminosity uncertainties.

the following equation:

$$\delta R_n = \frac{\delta\sigma_n}{\sigma_0}, \quad \text{with} \quad \sigma_0 = 248.4\ pb. \tag{32}$$

For completeness, Table 32 summarizes the measured cross sections, together with uncertainties due to statistics, systematics, and luminosity. Also listed is the number of fully corrected signal events for each jet multiplicity sample.

The cross section ratios with results from MCFM, CKKW, and PYTHIA MC simulations are compared in Table 33 and Figure 75. The matrix element generation of the CKKW samples was done up to jet multiplicities of 3. Higher jet multiplicities are due to parton showering and hadronization simulated with PYTHIA. We also show cross section ratios based on PYTHIA, which clearly illustrates the lack of higher order contributions at the hard scatter level.

Figure 76 compares jet p_T distributions for different jet multiplicities between data and MC (CKKW).

The results are in good agreement with QCD predictions.

Jet multiplicity	$\frac{\sigma(Z/\gamma^*(\to e^+e^-)+\geq nJets)}{\sigma_{Z/\gamma^*}}$ $[\cdot 10^{-3}]$	MCFM	CKKW	PYTHIA
≥ 1	120.1 $\pm$3.3(stat) $^{+15.6}_{-17.1}$(sys)	103.0	120.1	120.1
≥ 2	18.6 $\pm$1.4(stat) $^{+6.2}_{-5.0}$(sys)	18.9	21.4	15.4
≥ 3	2.8 $\pm$0.56(stat) $^{+1.43}_{-1.06}$(sys)	-	3.3	1.5
≥ 4	0.90 $\pm$0.44(stat) $^{+0.48}_{-0.40}$(sys)	-	0.40	0.12

Table 33: Comparison of measured cross section ratios with results from MCFM, CKKW, and PYTHIA.

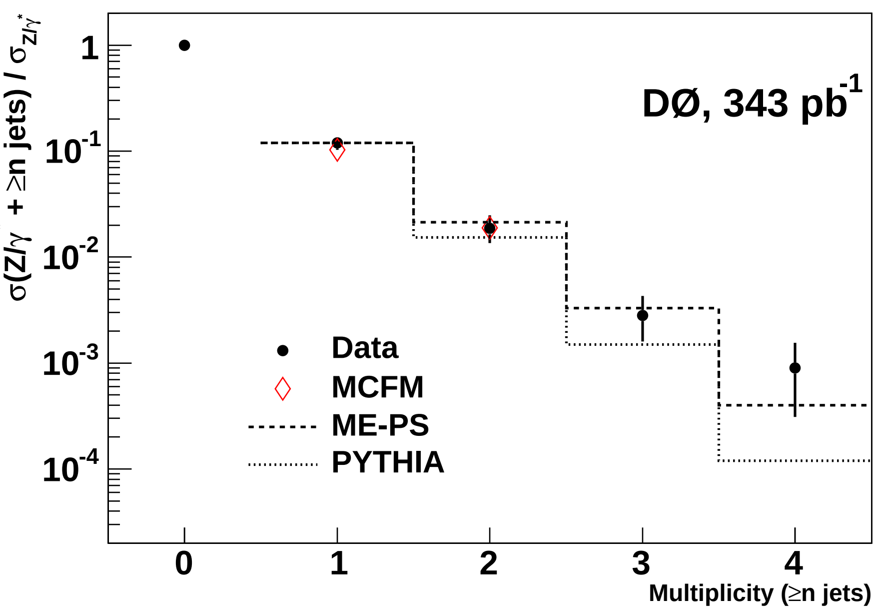

Figure 75: Ratios of the $Z/\gamma^*(\to e^+e^-)+\geq n$ jet cross sections to the total inclusive $Z/\gamma^* \to e^+e^-$ cross section versus n. The uncertainties on the data include the combined statistical and systematic uncertainties. The dashed line (CKKW) represents the predictions of LO matrix element calculations (MADGRAPH) using PYTHIA for parton showering and hadronization, normalized to the measured $Z/\gamma^*+\geq 1$ jet cross section ratio. The diamonds represent the MCFM predictions. The dotted line represents the PYTHIA prediction and is normalized to the measured $Z/\gamma^*+\geq 1$ jet cross section ratio.

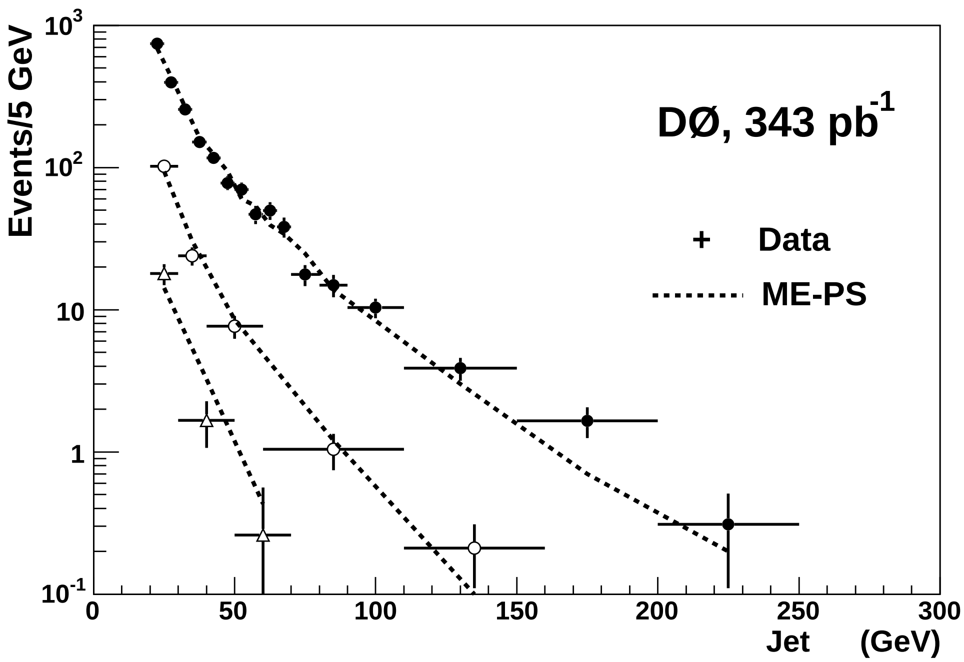

Figure 76: Data to theory (CKKW) comparison for the highest p_T jet distribution in the $Z+\geq 1$ jet sample, for the second highest p_T jet distribution in the $Z+\geq 2$ jet sample and for the third highest p_T jet distribution in the $Z+\geq 3$ jet sample. The errors on the data are only statistical.

10 Acknowledgments

We appreciate fruitful discussions with Gregorio Bernardi, Douglas Chapin, Suyong Choi, John Gardner, Avtandyl Kharchilava, Qizhong Li, Gustavo Otero, and Paul Telford.

We thank Suyong Choi for providing the MCFM cross sections and for generating the PYTHIA particle-level sample used in the analysis.

We also thank Steve Mrenna for providing the CKKW cross sections.

A Event Displays

Event displays for all events containing at least 4 jets.

A.1 Run 178159, Event 40565917, 5-jet event

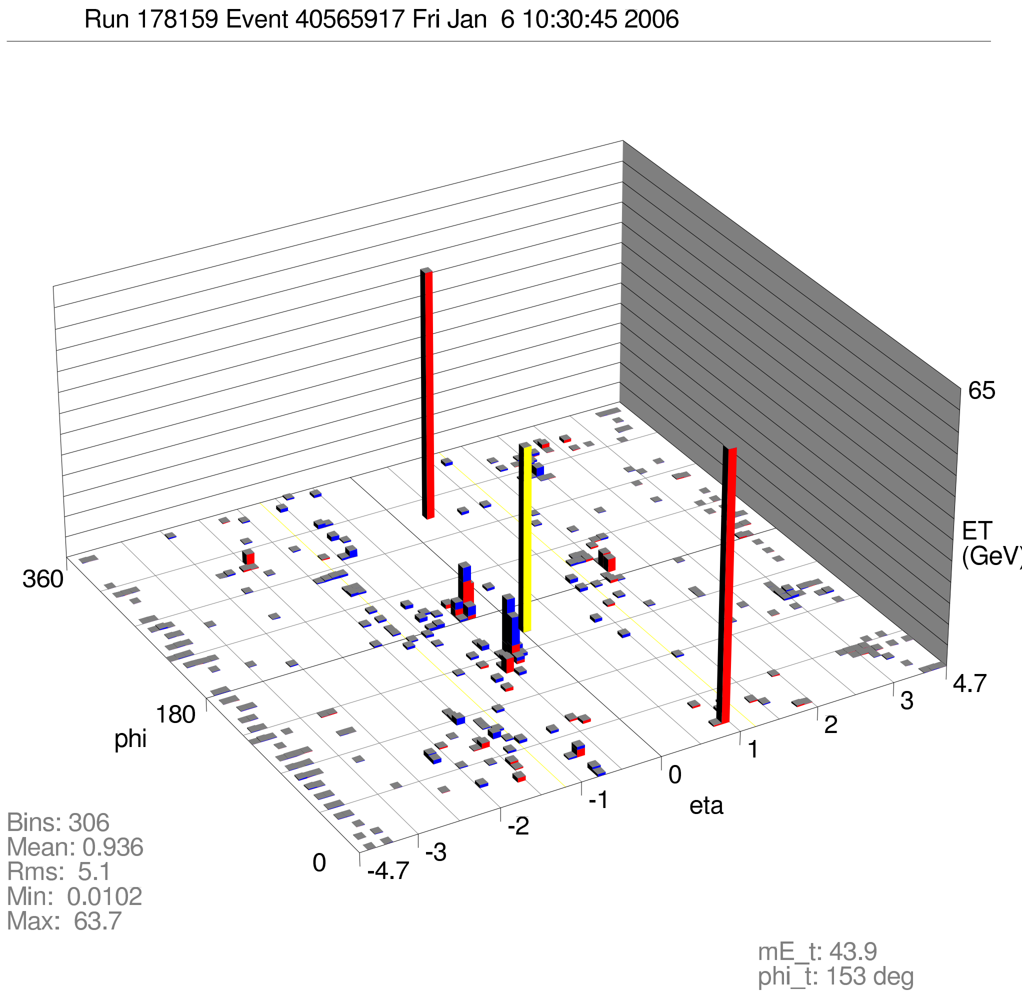

Figure 77: Lego Plot, Run 178159, Event 40565917, 5-jet event

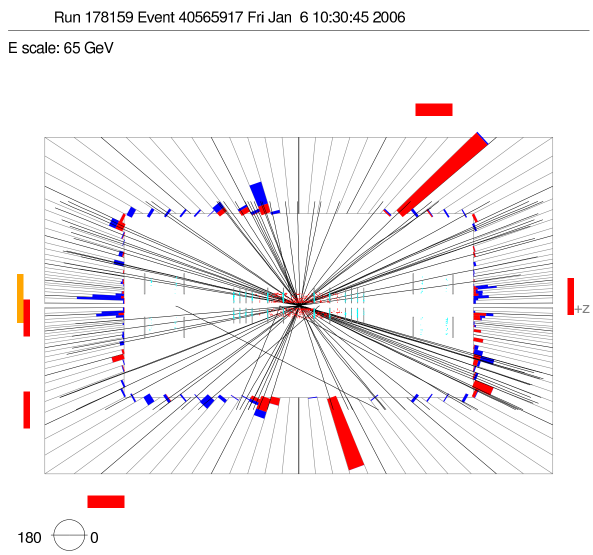

Figure 78: RZ View, Run 178159, Event 40565917, 5-jet event

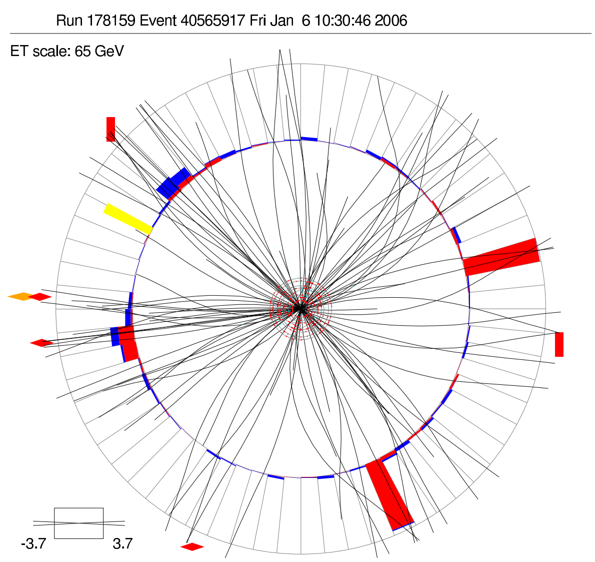

Figure 79: XY View, Run 178159, Event 40565917, 5-jet event

A.2 Run 167286, Event 26662632, 5-jet event

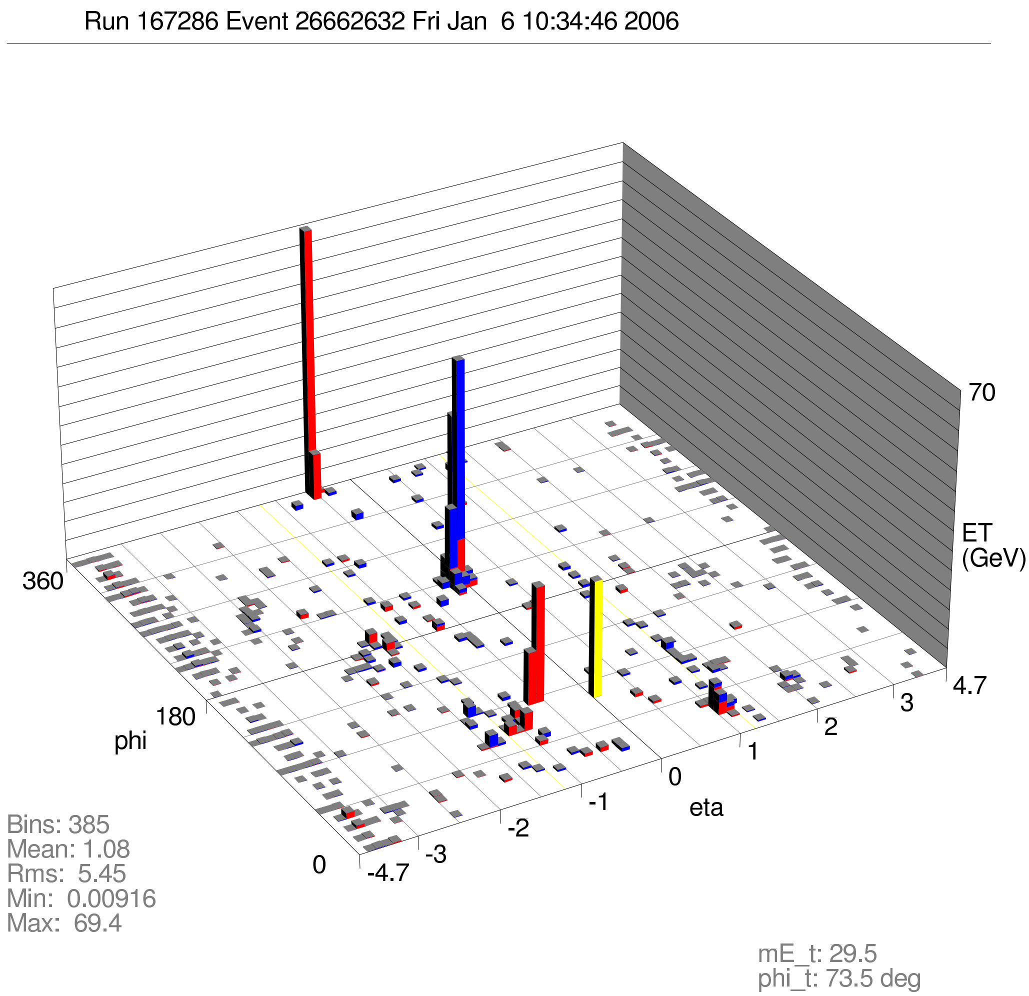

Figure 80: Lego Plot, Run 167286, Event 26662632, 5-jet event

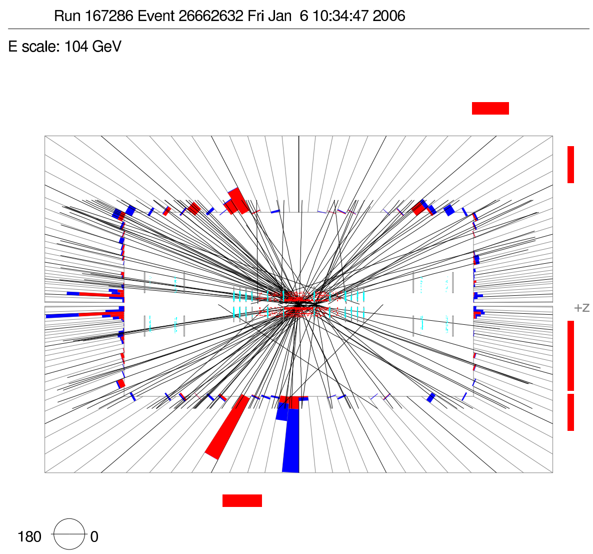

Figure 81: RZ View, Run 167286, Event 26662632, 5-jet event

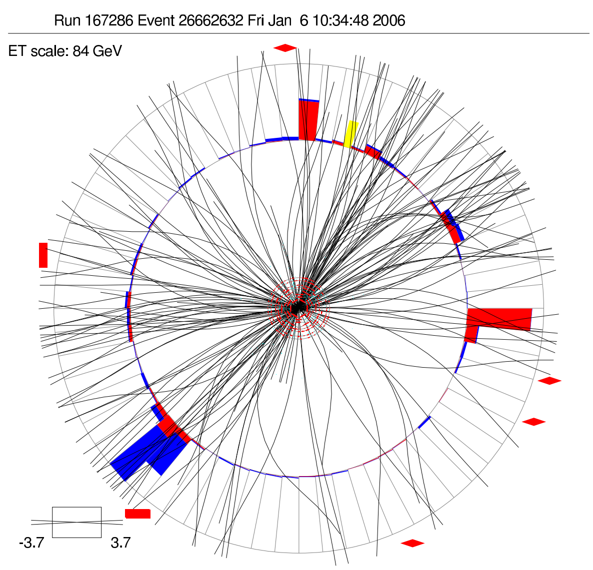

Figure 82: XY View, Run 167286, Event 26662632, 5-jet event

A.3 Run 179349, Event 46724452, 4-jet event

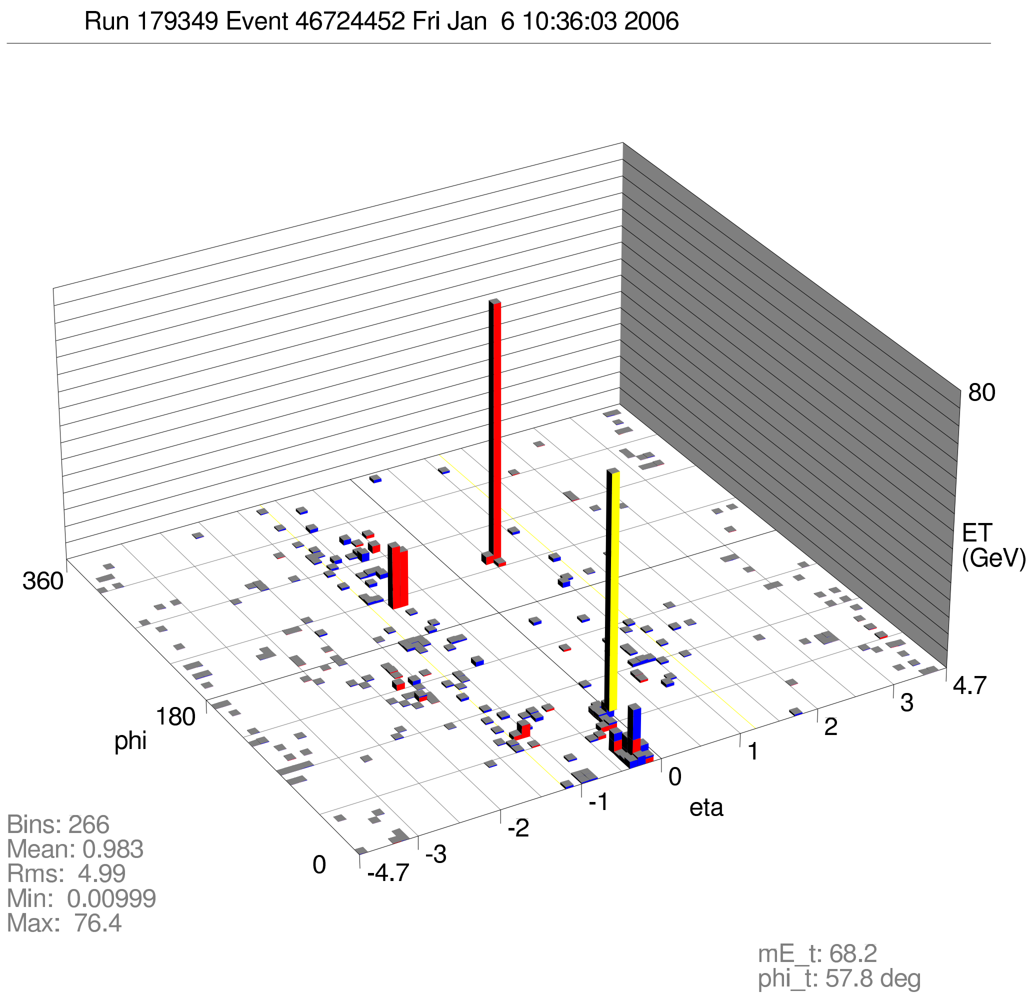

Figure 83: Lego Plot, Run 179349, Event 46724452, 4-jet event

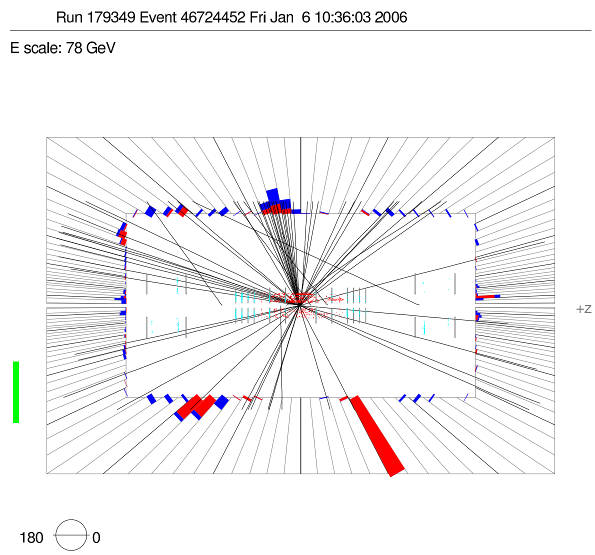

Figure 84: RZ View, Run 179349, Event 46724452, 4-jet event

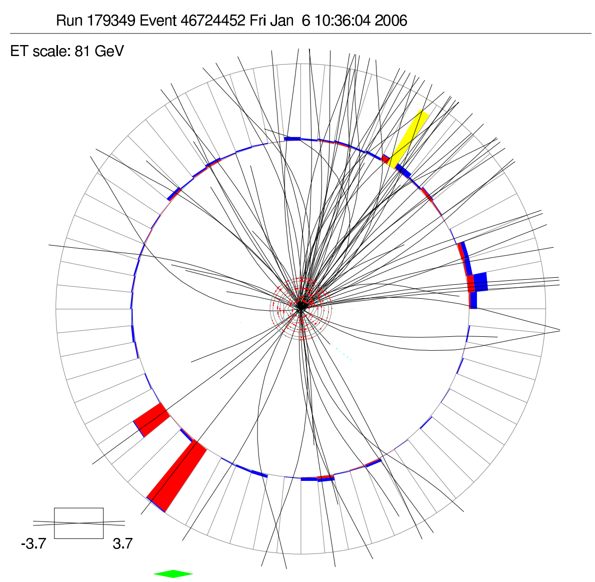

Figure 85: XY View, Run 179349, Event 46724452, 4-jet event

A.4 Run 179896, Event 24263189, 4-jet event

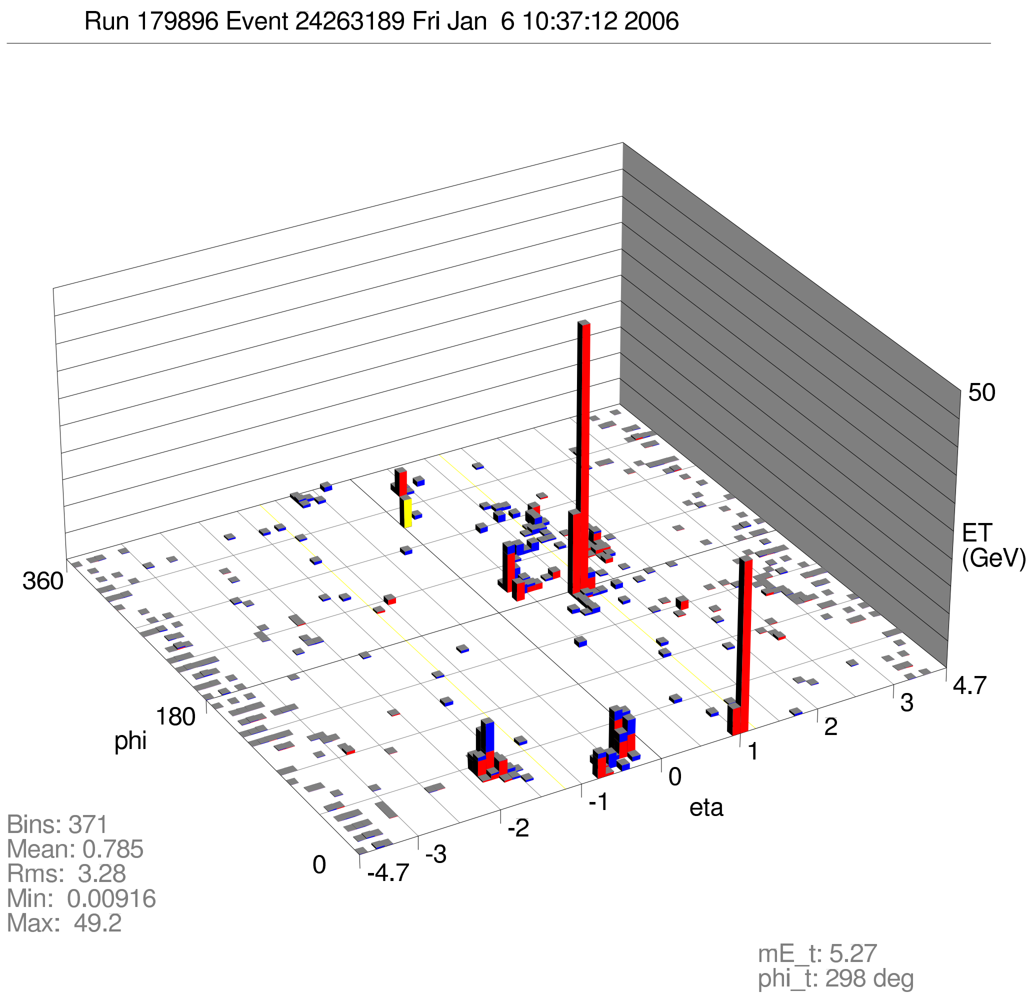

Figure 86: Lego Plot, Run 179896, Event 24263189, 4-jet event

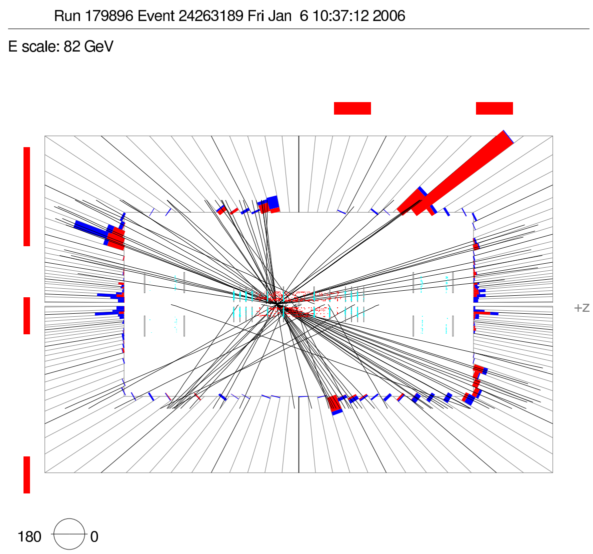

Figure 87: RZ View, Run 179896, Event 24263189, 4-jet event

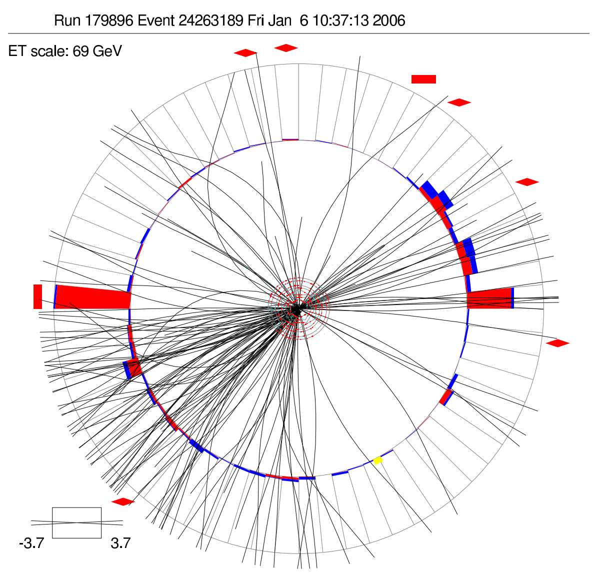

Figure 88: XY View, Run 179896, Event 24263189, 4-jet event

A.5 Run 177276, Event 11184476, 4-jet event

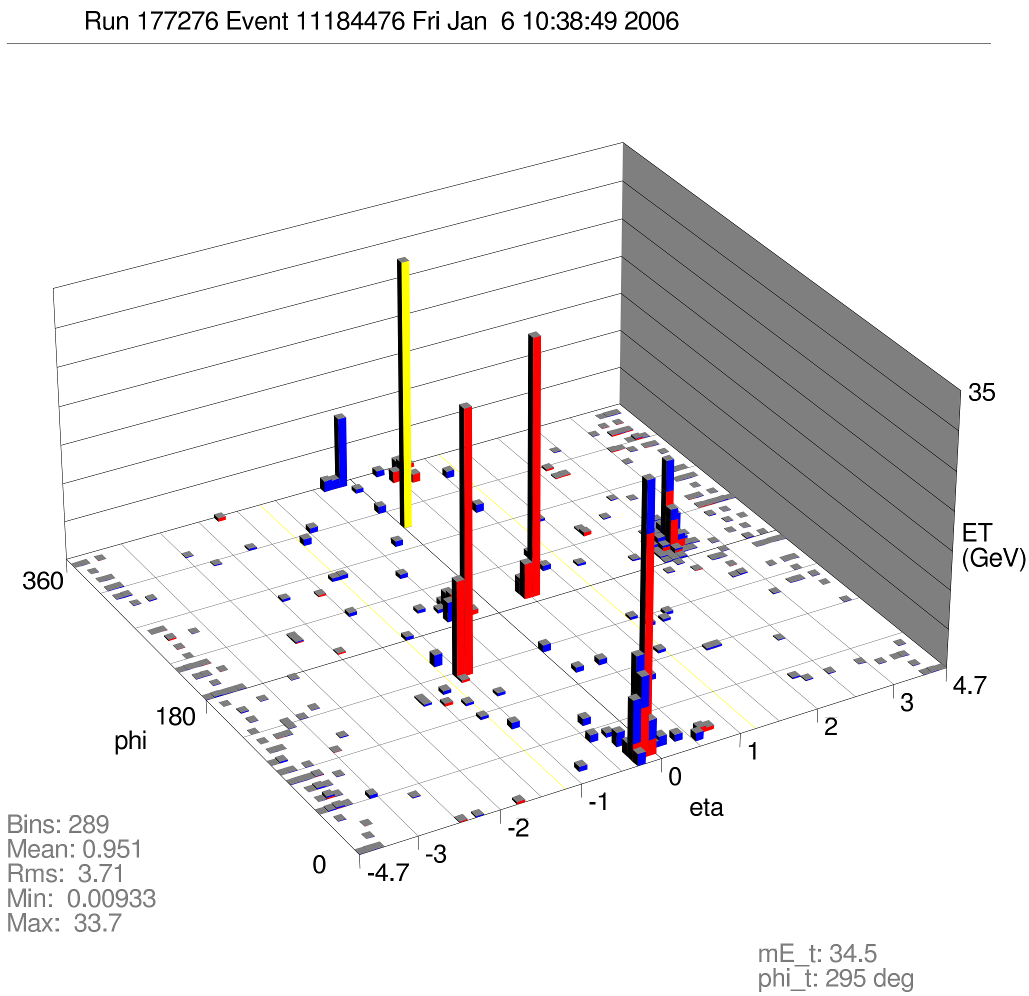

Figure 89: Lego Plot, Run 177276, Event 11184476, 4-jet event

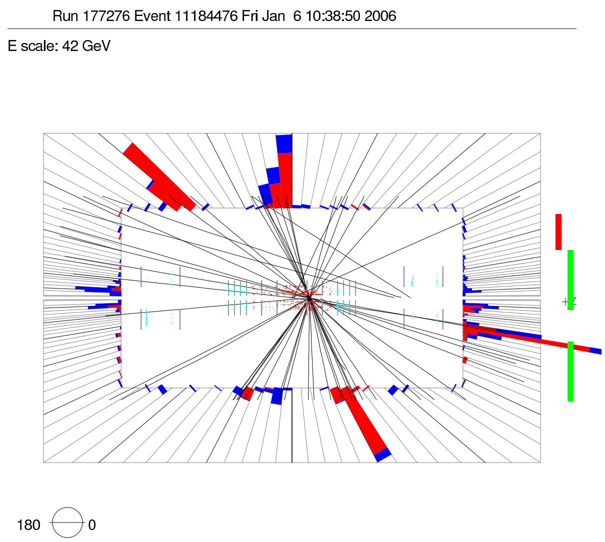

Figure 90: RZ View, Run 177276, Event 11184476, 4-jet event

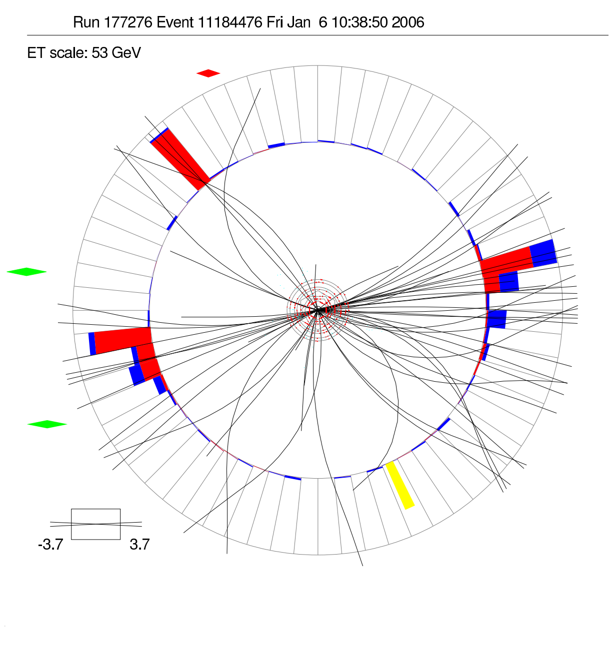

Figure 91: XY View, Run 177276, Event 11184476, 4-jet event

References

[1] D0 Collaboration, "The upgraded D0 Detector", http://www-d0.fnal.gov/Run2Physics/WWW/d0_private/reviews/Run2Det.pdf.

[2] U. Bassler et al., "Technical description of the T42 algorithm for the calorimeter noise suppression",

[3] http://www-d0.fnal.gov/~suyong/d0_private/athenaweb/athena.htm

D0 Note 4146, May 2003.

[4] http://www-clued0.fnal.gov/~alstone/D0Work/Athena/badruns/badruns.html

[5] http://www-d0.fnal.gov/Run2Physics/wz/d0-private/triggers/EMtriggers.html

[6] T. Sjöstrand et al., "PYTHIA 6.3 Physics and Manual", hep-ph/0308153, August 2003.

[7] L. Michelangelo et al., "ALPGEN, a generator for hard multiparton processes in hadronic collisions", hep-ph/0206293, June 2002.

[8] Supriya Jain, "Scale and Over-smearing for MC Electron", D0 Note 4402, March 2004.

[9] Top Physics Working Group, "D0 Top Analyses and Data Sample for the Winter Conferences 2004", D0 Note 4419, April 2004.

[10] F. Maltoni, "MADEVENT: Automatic Event Generation with MADGRAPH", hep-ph/0208156, August 2002.

[11] http://cepa.fnal.gov/personal/mrenna/Matched_Dataset_Description.html.

[12] S. Mrenna et al., "Matching matrix elements and parton showers with HERWIG and PYTHIA", JHEP05(2004)040, 2004.

[13] S. Catani et al., "QCD matrix elements + parton showers", JHEP11(2001)063, 2001.

[14] Private communication with Suyong Choi (suyong@fnal.gov) and http://mcfm.fnal.gov/.

[15] K. Ellis, "A critical review of vector boson + jets Monte Carlos", http://wwwcdf.fnal.gov/TevatronConnection/QCD_Theory_Keith.pdf.

[16] K. Ellis, "Method 2 at NLO", hep-ph/0405276, 2004.

[17] D. Chapin et al., "Measurement of the $Z \to e^+e^-$ and $W \to e^{\pm}\nu$ Production Cross Sections with $|\eta| < 1.05$", http://www-d0.fnal.gov/~gardnerj/wzcross_v3.2.pdf.

[18] Private communication with Paul Telford (ptelford@fnal.gov).

[19] CDF Collaboration, "First Measurement of Inclusive W and Z Cross Sections from Run II of the Tevatron Collider", Phys. Rev. Lett. 94, 091803 (2005), http://www-cdf.fnal.gov/physics/preprints/index.html.

[20] http://dzero.phy.uic.edu/james/higgs/index.html and
James Heinmiller, "Jet Reconstruction Efficiency", D0 Note 4837.

[21] Private communication with Mathieu Agelou (agelou@fnal.gov).

[22] T. Edwards et al., "Determination of the effective inelastic p anti-p cross-section for the D0 Run II luminosity measurement.", FERMILAB-TM-2278-E, November 2004.